Quantum Microwave Photodetection Using Superconducting Josephson Circuits.

by

Brendan Osberg

A thesis
presented to the University of Waterloo
in fulfillment of the
thesis requirement for the degree of
Master of Science
in
Physics

Waterloo, Ontario, Canada, 2009

I hereby declare that I am the sole author of this thesis. This is a true copy of the thesis, including any required final revisions, as accepted by my examiners.

I understand that my thesis may be made electronically available to the public.

Abstract

Superconducting circuits have recently become a major contender for the implementation of quantum computers owing to their compatibility with existing microchip fabrication technologies. Their utility stems largely from their ability to be coupled with resonant cavities for the purposes of trapping and relaying microwave radiation. Because of this feature, scientists are able to transmit quantum information from a variety of qubits. Though quantum-limited amplifiers exist, unfortunately there currently exists no microwave photon counter capable of single shot quantum detection.

Hence, we use superconducting circuits with Josephson junctions to design a microwave photon detector based on a modified phase qubit that exhibits a bandwidth of 4GHz, and a detection fidelity of 98%. We use metastable barrier transition (driven by incident photons) to create an avalanche effect analogous to current photo-diodes. Linear coupling of the junction flux with the radiation permits photodetection from an arbitrary quantum source in the GHz range. We show the device to be robust to changes in drive-frequency, temporal photon width, and resonator quality factor, and we optimize our device with respect to these parameters. We show the device to be stable over the necessary time scales, and yet sensitive enough to accurately measure photons on demand.

Acknowledgements

I would like to thank my committee members, Kevin Resch, Anton Burkov, and examiner Adrian Lupascu, as well as my supervisors Frank Wilhelm and Jay Gambetta for providing an excellent learning environment here at Waterloo. I thank the National Science and Engineering Research Council, and the Ontario Graduate Scholarship program as well as the University of Waterloo for providing financial support for this work. I thank SHARCNET for providing indispensable computer resources, as well as Jordan Kyriakidis for the same.

I thank QuantumWorks, and the Institute for Quantum Computing, for their support in providing a stimulating scientific environment in which to pursue research. I would also like to thank my group members, Peter Groszkowski, Felix Motzoi, Bill Coish, Ioana Serban and Farzad Qassemi for providing ideas and insight through daily discussion.

Finally, a special thank-you to my siblings Spencer Osberg and Natasha Scott, my friends Matt Molloy, Lesley Latham, Patrick Burgomaster, and Jillian Banfield as well as everyone at IQC and my Parents for all the personal support and encouragement that was necessary throughout this process.

Dedication

Dedicated to the memory of Dr. Masayoshi Senba, a great mentor and friend with a passionate and infectious sense of curiosity.

Contents

List of Figures

Chapter 1

Introduction

Research dating back to the 1980s[1, 2, 3] has demonstrated that macroscopic variables such as voltage and current can exhibit non-classical behaviour. Such quantum-mechanical phenomena can be seen using non-linear inductors (specifically, Josephson junctions) The energetics of which depend on the relative phase of the many-body electronic wave-function across the junction. Since then, the last two decades have brought about rapid evolution in the field of circuit quantum electrodynamics [4, 5, 6], and further research has shown the potential for coherent energetic coupling between the electrostatic properties of Josephson circuits and the electromagnetic modes of a resonant cavity [7, 8, 9, 10, 11]. Furthermore, the scientific community has explored increasingly broad avenues for development in this field ranging from pure mesoscopic science, to the wily challenges of quantum information processing.

Hence, it has been established that, just as optical photons represent a coupling mechanisms between the quantum states of atoms and molecules, microwave photons hold great potential for the coupling between 'artificial atoms' that can be fabricated on a microchip to serve as elementary building blocks for quantum computers [12]. For this reason, much work has been invested in the creation of non-classical radiation within on-chip superconducting circuit components. Indeed, with the generation of non-classical propagating fields [7], and the demonstrated potential for microwave radiation to act as a mediator in the coupling of solid state logic devices [4], the field of circuit quantum electrodynamics (CQED) has become a rapidly evolving test-bed for a wealth of mesoscopic quantum phenomena. One cumbersome deficiency within the established infrastructure, however, is the lack of a detector sensitive to single photons in the microwave regime.

While quantum-limited amplifiers exist [13, 14], single photon detectors with quantum sensitivity scale do not –an omission in the available resources for the implementation of quantum circuits which we seek to rectify. Single photon detectors have been proposed in parallel to this thesis [15], though the dependence of such detection on essential circuit and photon parameters has not been explored. Furthermore, there is a need within the community for a 'broadband' detector that

is not so sensitive to changes in the frequency of the photon; the above proposal, however, claims a bandwidth on the order of 'several MegaHertz', and a maximum detection probability of 50% [15]. We propose a detection scheme with a detection fidelity of over 98% and a bandwidth of 4 *Giga*Hertz –an improvement by a factor of over one-thousand in this criteria. Furthermore, the proposed model does not afford a natural reset mechanism, nor a clear accounting for the rate of spurious detections, or 'dark counts.' Here, we fully account for the rate of false-positive detection.

To reiterate, we present a new detection scheme vastly improved in both bandwidth and fidelity. We show the system to be robust to changes in all relevant parameters (such as the temporal width of the photon, the photon frequency, and the rate of dissipation) at an idealized metastable barrier height which we determine. We determine precisely the confidence with which the detector can be trusted to minimize spurious detection, and the time-scales over which detection processes occur; We show that it is possible to manage these effects and still detect microwave photons when present.

1.1 Outline.

In this thesis, we will introduce a series of increasingly detailed models to recreate the behaviour of Josephson circuits, using the initial, preliminary models to strengthen the credibility of the latter ones by corroborating some of the results from each.

- In chapter 2 we will introduce a common model for optical photo-detection [16] that provides the underpinnings for the numerical simulations we will use later. This model shows the basic excitation and evolution process that we are interested in in the trivial case of excitation into a band of levels with uniform energy spacing and coupling strength to the initial state.

- In chapter 3 we will introduce the eigenstates that we generate for the potential well created by our circuit (which, we shall see, takes the form of an asymmetric bistability.) We will show methods of energy-eigenstate solution based on the harmonic eigenstate basis, and on the discrete variable representation (DVR) [17], and explain why, in our circumstances, the latter is preferable.

- In chapter 4 we will restrict ourselves to purely classical simulations of the system, and we will consider driven anharmonic oscillations using the perturbative response theory [18]. In this model, we note the three resonance points in these results that serve to corroborate resonances observed in the quantum model which we will explore later. We will then proceed to calculate the dark escape rate using the metastable escape rate determined by Kramer [19, 20].

- Since the above calculations do not account for quantum tunnelling, in chapter 5 we introduce the imaginary part of the free energy and show how it can be used to calculate the escape rate, accounting for both thermal excitations, and quantum mechanical tunnelling. Since this method assumes instantaneous thermalization of the state's energy distribution, we cannot rely on this model for predictions of the dark current; we can, however, corroborate our estimates of the dark-current using mean first-passage time theory [21] in the high-damping limit.

- In chapter 6 we introduce our working model, exploiting the density matrix of states in the DVR basis determined from chapter 3. We introduce the various parameters that require optimization for a detector, such as the temporal pulse width, resonator quality factor, photon frequency, and barrier height and we scan through these parameters to determine both the false and true positive detection probabilities of our system.

  At the optimal parameters, we determine a bandwidth of 4 GHz and we characterize the range of our sensitivity to variations in the other pertinent parameters (such as the temporal width of the photon wave-packet, and the dissipation rate of the circuit.) The robustness of our detection scheme is a key selling point of our model, and in chapter 6 we optimize our detector to assure maximal true positive detection probability, and minimal false-positive probability. As we shall see, this can be achieved with a great deal of flexibility in the aforementioned parameters.

- Finally, in chapter 7 we provide a discussion and summary of the key findings in the above.

Before delving into the dynamics of our Josephson circuit, however, we consider a simplified model of photo-detection used in the optical regime [16], and compare analytic results obtained from perturbation theory with computational results. The agreement between the two will serve to establish confidence in the computational techniques that will be employed later.

Chapter 2

A conventional optical photo-detection model

We consider a stable initial quantum state with a band of unoccupied energy levels above it, separated from the former by energy ω_0 with internal energy separation $\mathrm{d}\omega$. A photon with frequency ω_R ('R' for '*Radiation*') is incident upon the system, and we wish to model the probability that the state will be excited into the band of levels above it (see figure 2.1 for schematic illustration.)

We treat the electromagnetic field as a classical source, while the states of the system are quantum-mechanically discretized. We define our probability of excitation by applying the time evolution operator to the initial state, and by determining the consequent amplitudes of the system in each of the states above the initially populated one (we refer to these levels collectively as 'the band'.) That is to say: given N states (including the initial state) for integer f, where $|f\rangle$ is the f^{th} energy eigenstate of the whole system,

$$P_E(t) = \sum_{f=1}^{N} |\langle f|\hat{U}_1(t)|0\rangle|^2. \tag{2.1}$$

Naturally, then, the probability of *non*-excitation is given by

$$P_{NE}(t) = |\langle 0|\hat{U}_1(t)|0\rangle|^2. \tag{2.2}$$

Here $\hat{U}_1(t)$ is the time evolution operator due to the perturbation introduced to the system from the incident photon. We will first evaluate this probability with a perturbative method[16] by approximating the time evolution operator $\hat{U}$ over short time scales. We will then analyze the system using more precise numerical techniques –the latter of which will mirror our final approach in chapter 6 much more closely.

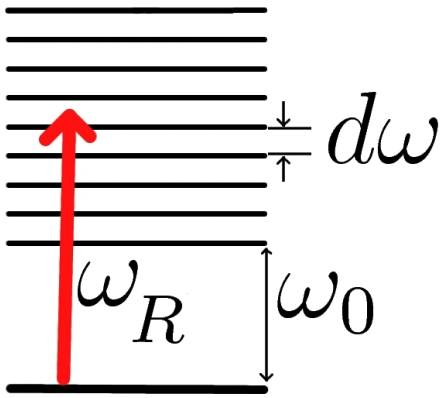

Figure 2.1: Graphical representation of the excitation process due to radiation with frequency ω_R. The initial state undergoes transition across an energy gap ω_0 into a band with level spacing $d\omega$, the timescale of this excitation and the distribution amongst each of the states in the band is discussed herein. For the sake of concreteness, let us assume all frequencies are in units of 10^9 radians per second.

2.1 Perturbative approach

The time evolution operator $\hat{U}_1(t)$ evolves a quantum state from some point in time (presumably $t = 0$) to time 't' and is defined by

$$|\Psi(t)\rangle = \hat{U}_1(t)|\Psi(0)\rangle \tag{2.3}$$

where our state $|\Psi(t)\rangle$ is defined in the interaction frame. Assuming the photon in our detection system gives rise to a Hamiltonian interaction $H_1(t)$ (also in the interaction frame,) the Schrödinger differential equation describing its evolution is given by:

$$\frac{\mathrm{d}}{\mathrm{dt}}|\Psi\rangle = \frac{-\mathrm{iH_1(t)}}{\hbar}|\Psi\rangle \tag{2.4}$$

If we substitute $|\Psi(t)\rangle = \hat{U}_1(t)|\Psi(0)\rangle$ into (2.4) we see that

$$\frac{\mathrm{d}}{\mathrm{dt}}\left[\hat{U}_1(t)|\Psi(0)\rangle\right] = \frac{-\mathrm{i}\hat{\mathrm{H}}_1(\mathrm{t})}{\hbar}\left[\hat{U}_1(t)|\Psi(0)\rangle\right] \tag{2.5}$$

$$\hat{U}_1(t)\frac{\partial}{\partial t}|\Psi(0)\rangle + |\Psi(0)\rangle\frac{\partial}{\partial t}\hat{U}_1(t) = \frac{-\mathrm{i}\hat{\mathrm{H}}_1(\mathrm{t})}{\hbar}\left[\hat{U}_1(t)|\Psi(0)\rangle\right] \tag{2.6}$$

We assume that all time dependence is manifested in the operator $\hat{U}(t)$, and that therefore the first term in (2.6) is zero, consequently

$$\frac{\partial}{\partial t}\hat{U}_1(t) = \frac{-\mathrm{i}\hat{\mathrm{H}}_1(\mathrm{t})}{\hbar}\hat{U}_1(t). \tag{2.7}$$

Integrating this equation results in expressions involving $\hat{U}_1(t), \hat{U}_1(0)$. If we recognize that evolving through a period of time zero amounts to no change in the state (and that such an operator is therefore equivalent to the identity operator) this expression is equivalent to:

$$\hat{U}_1(t) = 1 - \frac{\mathrm{i}}{\hbar}\int_0^t H_1(t')\hat{U}_1(t')dt' \tag{2.8}$$

One can then place the expression for $\hat{U}_1(t)$ on the left in the term on the right, recursively generating higher-order terms in dt' to define $\hat{U}_1(t)$ in terms of $\hat{H}_1(t)$. For example:

$$\begin{aligned}\hat{U}_1(t) = 1 + \frac{-\mathrm{i}}{\hbar}\int_0^t H_1(t')dt' + \left(\frac{-\mathrm{i}}{\hbar}\right)^2\int_0^t dt'\int_0^{t'} dt''H_1(t')H_1(t'') \\ + \left(\frac{-\mathrm{i}}{\hbar}\right)^3\int_0^t dt'\int_0^{t'} dt''\int_0^{t''} dt'''H_1(t')H_1(t'')H_1(t''') + \ldots\end{aligned} \tag{2.9}$$

This is often referred to as the Dyson series expansion of time-ordered perturbation. Note that each successive term involves a higher-order term of dt; hence, for short time-intervals, we will take expression 2.9 only to first order (i.e. we will consider only the first two terms.)

In our case, the perturbing Hamiltonian that causes the excitation described above is given as $H_1(t) = I(t)\phi(t)$[22], where $I(t)$ is the current being driven through the system, and $\phi(t)$ is the flux (the flux is written in time-dependent form because our analysis is confined to the interaction frame.) Equation (2.1), evaluated using first-order time evolution as in (2.9) then corresponds to

$$P_E(t) = \sum_{f=1}\left|\langle f|\left(1 - \frac{\mathrm{i}}{\hbar}\int_0^t I(t')\hat{\phi}(t')dt'\right)|0\rangle\right|^2. \tag{2.10}$$

Since the initial state is defined to be orthogonal to the band of levels, the unity term in expression (2.8) yields precisely zero. To calculate the contribution from the second term we express the operator $\hat{\phi}(t)$ in a more convenient form. This can be accomplished using an expansion in the eigenstate basis $|n\rangle, |m\rangle$ as

$$I(t)\hat{\phi}(t) = I(t)\sum_{n,m}\hat{U}_0^\dagger|n\rangle\langle n|\hat{\phi}|m\rangle\langle m|\hat{U}_0 \tag{2.11}$$

where $\hat{U}_0 = \mathrm{e}^{\left[-\mathrm{i}\frac{\hat{\mathrm{H}}_0 \mathrm{t}}{\hbar}\right]}$, is the time-evolution mapping between Schrödinger and interaction frames, and $\hat{H}_0$ is the unperturbed Hamiltonian of the system (of which $|n\rangle$, and $|m\rangle$ are eigenstates.) It follows then that

$$\begin{aligned} I(t)\hat{\phi}(t) &= I(t)\sum_{n,m}\phi_{nm}\hat{U}_0^{\dagger}|n\rangle\langle m|\hat{U}_0 \\ &= I(t)\sum_{n,m}\phi_{nm}\mathrm{e}^{\left[\frac{\mathrm{i}\hat{\mathrm{H}}_0 \mathrm{t}}{\hbar}\right]}|n\rangle\langle m|\mathrm{e}^{\left[\frac{-\mathrm{i}\hat{\mathrm{H}}_0 \mathrm{t}}{\hbar}\right]} \\ &= I(t)\sum_{n,m}\phi_{nm}\mathrm{e}^{\left[\mathrm{i}\frac{(\epsilon_\mathrm{n}-\epsilon_\mathrm{m})\mathrm{t}}{\hbar}\right]}|n\rangle\langle m| \end{aligned} \tag{2.12}$$

where ϕ_{nm} are time *independent*, and ϵ_n, ϵ_m are the eigen-energies of state $|n\rangle, |m\rangle$ respectively. We assume $I(t)$ has the form $I(t) = I_0 \sin(\omega_R t)$, Applying the result obtained in (2.12) to (2.10) we arrive at

$$\begin{aligned} P_E(t) &= \sum_{f=1}\left|\langle f|\left(\frac{\mathrm{i}}{\hbar}\int_0^t I(t')\sum_{n,m}\phi_{nm}\mathrm{e}^{\left[\mathrm{i}\frac{(\epsilon_\mathrm{n}-\epsilon_\mathrm{m})\mathrm{t}'}{\hbar}\right]}|n\rangle\langle m|dt'\right)|0\rangle\right|^2 \\ &= \sum_{f=1}\left|\frac{-\mathrm{i}}{\hbar}\int_0^t I(t')\phi_{f0}\mathrm{e}^{\left[\mathrm{i}\frac{(\epsilon_\mathrm{f}-\epsilon_0)\mathrm{t}'}{\hbar}\right]}\mathrm{dt}'\right|^2 \\ &= \sum_{f=1}\frac{I_0^2|\phi_{f0}|^2}{\hbar^2}\left|\int_0^t \sin(\omega_R t')\mathrm{e}^{[\mathrm{i}\omega_{\mathrm{f}0}\mathrm{t}']}\mathrm{dt}'\right|^2. \end{aligned} \tag{2.13}$$

In any realistic system, of course, ϕ_{f0} would become negligibly small for very large 'f'; for the moment we assume that ϕ_{f0} is constant (unity) over the band of levels considered, and zero elsewhere. For compactness, we define $\gamma_f(t)$ as

$$\begin{aligned} \gamma_f(t) &\equiv \left|\int_0^t \sin\left(\omega_R t'\right)\mathrm{e}^{\left[\mathrm{i}\frac{\omega_{\mathrm{f}0}\mathrm{t}'}{\hbar}\right]}\mathrm{dt}'\right|^2 \\ &= \Big(\omega_R^2\left[1+\cos^2(\omega_R t)\right] + \omega_{f0}^2\left[1-\cos^2(\omega_R t)\right] \\ &- 2\left[\omega_R^2\cos(\omega_R t)\cos(\omega_{f0}t) + \omega_R\omega_{f0}\sin(\omega_R t)\sin(\omega_{f0}t)\right]\Big)\left(\omega_R^2-\omega_{f0}^2\right)^{-2}. \end{aligned} \tag{2.14}$$

Hence, we express (2.10) in the form

$$P_E(t) = \sum_{f=1}\frac{\gamma_f(t) I_0|\phi_{f0}|^2}{\hbar^2}. \tag{2.15}$$

This is our perturbative excitation probability; it does not conserve probability, and is valid only on short time scales. In the following section we will derive methods of obtaining more precise probabilities through computational methods, and compare the results of each.

2.2 Numerical approach

We now consider a more precise calculation of the probability of excitation. We begin with the Schröedinger equation as in (2.4) with the same Hamiltonian as in 2.12. We represent the state as a combination of energy eigenstates $|p\rangle$

$$|\Psi\rangle = \sum_p c_p(t)|p\rangle \tag{2.16}$$

where $c_p(t)|_{t=0} = \delta_{0p}$. Substituting this into (2.4) in conjunction with (2.12) yields:

$$\frac{\partial}{\partial t}\left(\sum_p c_p(t)|p\rangle\right) = \frac{-\mathrm{i}}{\hbar} I(t) \sum_{n,m} \phi_{nm} \mathrm{e}^{\left[\mathrm{i}\frac{(\epsilon_\mathrm{n}-\epsilon_\mathrm{m})\mathrm{t}}{\hbar}\right]} |n\rangle\langle m| \left(\sum_q c_q(t)|q\rangle\right). \tag{2.17}$$

Therefore (taking the inner product with $\langle n|$):

$$\frac{\partial}{\partial t} c_n(t) = \frac{-\mathrm{i}}{\hbar} I(t) c_m(t) \sum_m \phi_{nm} \mathrm{e}^{\left[\mathrm{i}\frac{(\epsilon_\mathrm{n}-\epsilon_\mathrm{m})\mathrm{t}}{\hbar}\right]} \qquad \forall \quad n. \tag{2.18}$$

In principle, for a system involving $(N-1)$ states in the band, in addition to the initial state, the N coupled differential equations corresponding to (2.18) describe the time-evolution of the system entirely. In practise, equation (2.18) is broken up into real and imaginary components yielding the $2N$ differential equations given as:

$$\frac{\partial}{\partial t}\mathrm{Re}\left\{\mathrm{c_n(t)}\right\} = \frac{\mathrm{I(t)}}{\hbar} \sum_\mathrm{m} \left[\mathrm{Im}\left\{\mathrm{c_m(t)}\right\} \cos\left((\epsilon_\mathrm{n}-\epsilon_\mathrm{m})\mathrm{t}\right) + \mathrm{Re}\left\{\mathrm{c_m(t)}\right\} \sin\left((\epsilon_\mathrm{n}-\epsilon_\mathrm{m})\mathrm{t}\right)\right] \phi_\mathrm{nm}$$

$$\frac{\partial}{\partial t}\mathrm{Im}\left\{\mathrm{c_n(t)}\right\} = \frac{\mathrm{I(t)}}{\hbar} \sum_\mathrm{m} \left[-\mathrm{Re}\left\{\mathrm{c_m(t)}\right\} \cos\left((\epsilon_\mathrm{n}-\epsilon_\mathrm{m})\mathrm{t}\right) + \mathrm{Im}\left\{\mathrm{c_m(t)}\right\} \sin\left((\epsilon_\mathrm{n}-\epsilon_\mathrm{m})\mathrm{t}\right)\right] \phi_\mathrm{nm}. \tag{2.19}$$

These equations can be solved numerically using the Runge Kutta optimized coupled differential equation solver, implemented in the GNU standard library software package [23]. By taking the squared modulus of each of these amplitudes we

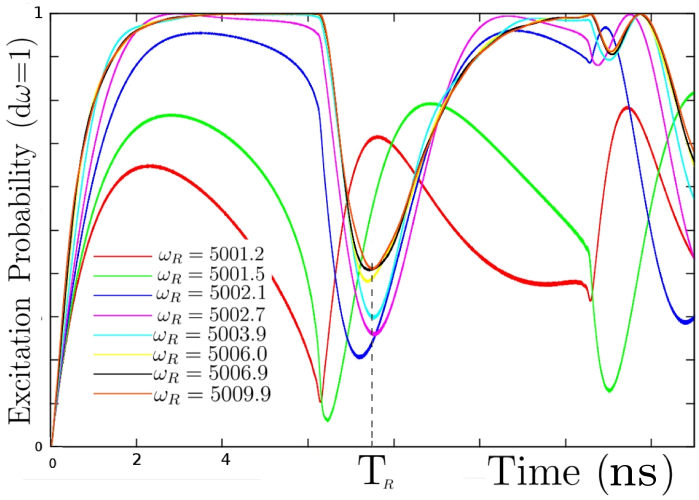

Figure 2.2: Probability of excitation into the band of levels described above. An initial state seperated by energy ω_0 ($\hbar = 1$) from a band of levels with unity level and coupling driven at various frequencies ω_R. All frequencies are in units of rad s^{-1}. We observe that the excitation probability is relatively independent of ω_R, provided ω_R is tuned to excitation well within the energy band of the band (i.e. boundary effects come into play as ω_R approaches ω_0 or $(\omega_0 + Nd\omega)$). The brief dip in probability occurs at a point termed the 'Recurrence time' and is a function of the level spacing, $d\omega$, only.

can assess the probability as a function of time that the state is excited into the band.

$$P_E(t) = \sum_{n=1} |c_n(t)|^2. \tag{2.20}$$

For example, assuming $I(t) = I_0 \sin(\omega_R t)$, and setting $\hbar = I_0 = \mathrm{d}\omega = 1$, $\omega_0 = 5000$, and assuming $N = 50$ states, the probability of excitation as a function of time for various driving frequencies ω_R is shown in figure 2.2 Note the recurrence time 'T_R' evident in the figure. Since the initial state oscillates between the different states within the band at different frequencies, we attribute this brief 'dip' to momentary phase-matching between the various cycles. The dependence of the recurrence time on the energy level spacing of the band is shown in figure 2.3

Furthermore, the distribution of probabilities within the band is shown in figure 2.4. Note the peak at the tuning level (i.e. the state closest in energy to ω_R above the initial state) as well as the decreasing 'sharpness' of the peak in energy distribution with increasing time. Naturally, this is the result of state excitation being closely tuned to one region of levels, and then dispersing outward from it (in the absence of dissipation.)

Finally, the probability of excitation (as defined in (2.1)) using the computation

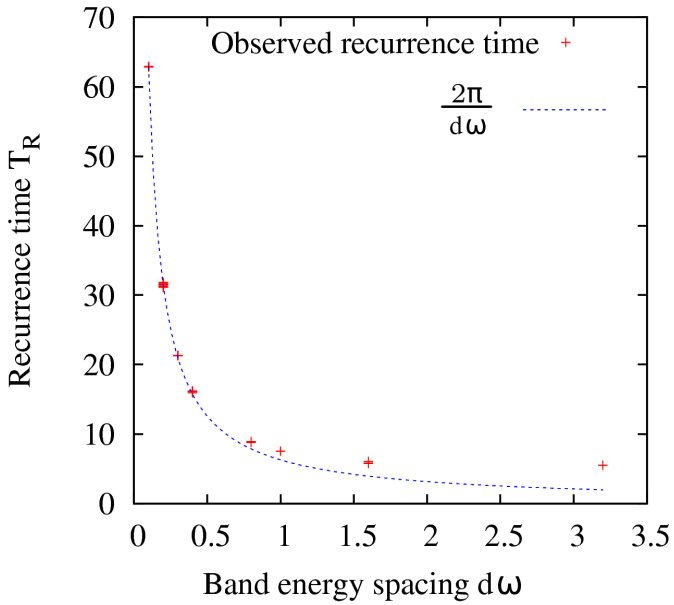

Figure 2.3: Recurrence time as a function of band level spacing. For each value of $d\omega$, 5 different driving frequencies were selected using random number generation confined to tuning within the middle 75% of the band. In many cases the resulting data were so consistent that they have the appearance of a single datum; this demonstrates that the excitation is independent of the driving frequency, and that recurrence time is inversely proportional to level spacing.

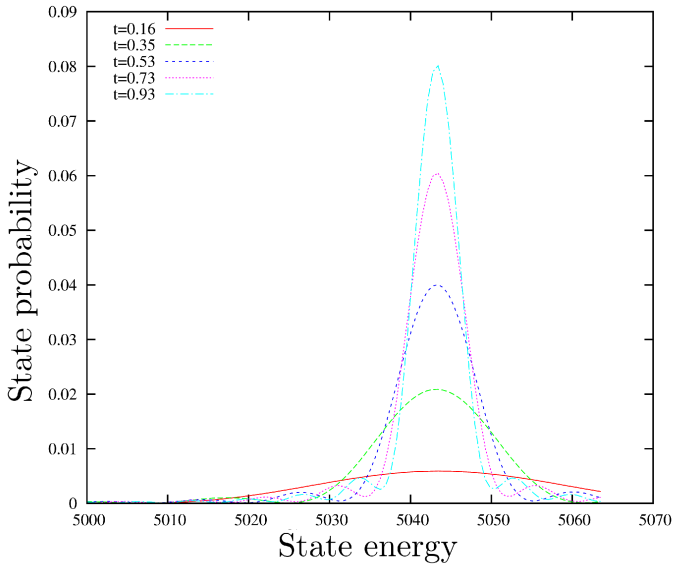

Figure 2.4: Probability distribution amongst the states in the band for given tuning and level spacing - these results are typical. Excitation is tuned to a small subset of levels, from which population gradually disperses.

results from the coefficients c_n can be directly compared with the results of equation (2.15) -with the latter referred to as the 'Perturbative solution.' Figure 2.5 shows a typical comparison between the two results for two values of $d\omega$, each with the same driving frequency for the two models. The agreement is evident and representative, and serves to validate the numerical approach that we will employ in subsequent chapters.

2.3 Discussion

In the preceding, we analyzed photo-excitation from an initial state into a band of energy eigenstates from the incidents of a photon with characteristic frequency. We show a short-term perturbative model for excitation, as well as a direct numerical evaluation of the coupled differential equations describing the amplitudes of the evolving system in each of the energy eigenstates. We show that on short time scales the two methods have excellent agreement, and that in the latter case, probability distribution throughout the states satisfies normalization constraints.

Furthermore, although the drive frequency determines the peak in the energy spectrum of the excitation probability of the states, the *overall* excitation probability is independent of the driving frequency. This is important since any real photon will be made up of a range of frequencies associated to a wave-packet -however it should be noted that this model assumes equal coupling of the initial state to all

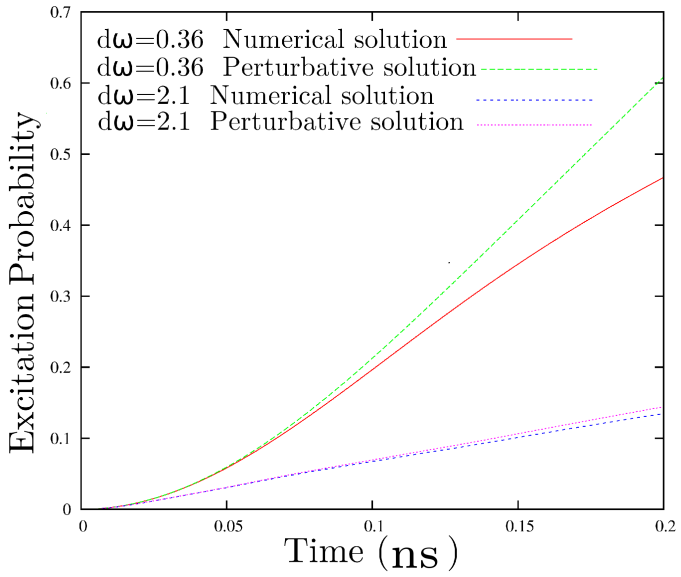

Figure 2.5: Typical probabilities of excitation as a function of time using the results of (2.15), and (2.20). The results of (2.15) show strong agreement for short time intervals, but develop errors that scale with t^2, and eventually violate normalization. Equation (2.18) however, maintains normalization; the fact that it agrees with the predictions of (2.15) over short time scales reinforces our confidence in it.

levels in the band -an assumption that will *not* hold in the model we employ in chapter 6. We also show that the recurrence time is inversely proportional to the level spacing of the band; this will be a useful relationship since we wish to engineer our system such that dissipative effects take place on a shorter time scale than recurrence. Describing the full dynamics of state relaxation and dissipation will require making use of density matrices instead of amplitude coefficients, however the treatment will employ is very much analogous to equation (2.19).

When we consider the physics of photodetection, involving irreversible dissipation, our numerical simulations will more closely resemble the form:

$$\frac{\mathrm{d}}{\mathrm{dt}}\rho_{nm}(t) = -\mathrm{i}\sum_{\mathrm{j}} \mathrm{H}_{nj}\rho_{jm} + \mathrm{i}\sum_{j} \mathrm{H}_{jm}\rho_{nj} + \kappa\rho_{n+1,m+1}\sqrt{(n+1)(m+1)} - \frac{\kappa}{2}n\rho_{nm} - \frac{\kappa}{2}m\rho_{nm}. \tag{2.21}$$

The latter terms in (2.21) describe the de-excitation process by which the system emits its energy to the environment where κ represents a phenomenological constant. An actual photodetection process will necessarily involve considering states with energy below the prepared state, into which the band of levels irreversibly decay.

Of course the simplifications of this model are evident. In our actual system the initial state will not exhibit uniform coupling with the energy levels above it, and those levels will not be of uniform spacing. Hence, the next step in building a more realistic model is resolving the energy eigenstates that exist within our bounded potential, and determining the coupling strength of each to the initial state.

Chapter 3

System energetics

We return now from our consideration of existing photo-detection schemes in the optical regime to the microwave system of our interest. We pause here to consider the coupling of microwave wave-guide with our device, and the delivery of radiative power from the former to the latter. We then present the Hamiltonian we will employ to determine the energy eigenstates of our detector in the absence of any disturbing drive from an incident photon. These states will not only determine the spontaneous escape rate (or dark count rate) in the absence of photonic drive, but they will also form the basis of time evolution for our density matrix as we will see in chapter 6.

3.1 Our proposed circuit.

We begin by considering the circuit of parallel components shown in figure 3.1; the circuit consists of a Josephson junction, a linear, externally biased inductor, and a resistor to encapsulate the effects of the surrounding thermal bath. The former components will determine the energy eigenstates of our model, while the effects of the latter will be captured in the time dynamics of our system via bath-induced transitions between the energy eigenstates (see chapter 6.) To determine the energy eigenstates of this system, we introduce the reduced branch flux,

$$\phi = \frac{2\pi}{\Phi_0}\Phi = \frac{2\pi}{\Phi_0}\int_{-\infty}^{t} v(t')dt' \tag{3.1}$$

and branch charge

$$q = \frac{\Phi_0}{2\pi\hbar}Q = \frac{\Phi_0}{2\pi\hbar}\int_{-\infty}^{t} I(t')dt' \tag{3.2}$$

where Q, and Φ are as defined by Devoret [24]. In equations 3.1 and 3.2 we have used $v(t)$ and $I(t)$, the voltage and current, respectively across the Josephson

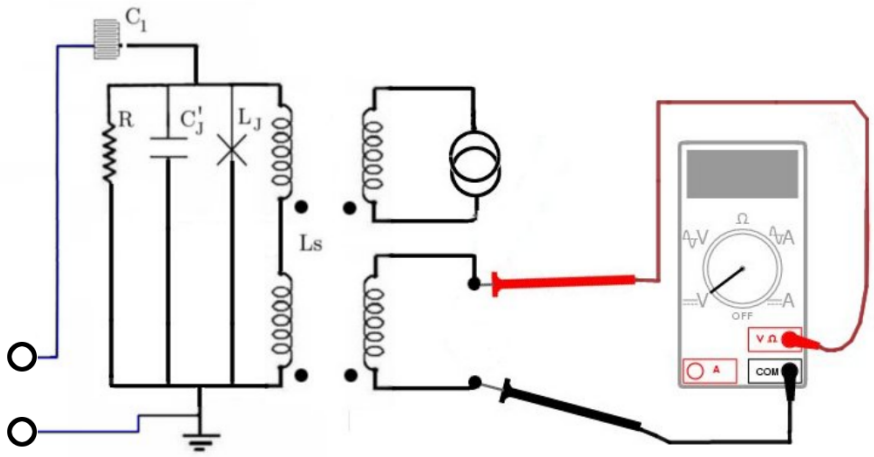

Figure 3.1: Schematic of the Josephson circuit coupled via capacitor C_1 to the cavity resonator. State changes in any qubit coupled to this transmission line cavity generate cavity modes which induce current flow through the circuit -our detector. The circuit consists of a parallel combination of a linear, externally biased inductors with a collective effective inductance L_S, a Josephson junction (which we model using a non-linear inductor L_J, and a capacitor C'_J,) and a resistor to account for dissipation.

element at time t, and $\Phi_0 = \frac{h}{2e}$, the flux quantum. We will see in a moment, why these parameters play such an important role, and why it is convenient to use the dimensionless parameters q and ϕ instead of the generalized charge Q and flux Φ. Neglecting, for the moment, the thermal bath surrounding the system, we observe an asymmetric bistability in the above model [25] resulting from the free, or undriven Hamiltonian[6] which takes the form

$$\begin{aligned} \hat{H}_0 &= \frac{\hat{Q}^2}{2C_J} + \frac{\left(\hat{\Phi} - \Phi_x\right)^2}{2L_s} - E_J \cos\left(\frac{2\pi\hat{\Phi}}{\Phi_0}\right) \\ &= E_J\left(\frac{E_c}{E_J}\hat{q}^2 + \frac{(\phi - \phi_x)^2}{2\beta} - \cos(\hat{\phi})\right). \end{aligned} \tag{3.3}$$

In equation 3.3 E_J is the Josephson energy $I_c\Phi_0/(2\pi)$ (I_c is the critical current of the junction[1]), $E_c = 2e^2/C_J$ is the charge energy, and ϕ_x is the effective biasing flux introduced to the circuit via its coupling to the control applied as shown in figure 3.1. It has been shown[6] that for the many-body electronic wave-function, $\left[\hat{\phi}, \hat{q}\right] = \mathrm{i}$; hence, equation 3.3 can be conveniently treated with the same 'momentum-position' paradigm that has been employed to solve for the wave equation of electrons and other particles. The precise position, or flux, wave-functions of our energy eigenstates will be explored later in this chapter. The interaction of the circuit with the current driven by the incident photon will be captured by the standard atom-photon dipole interaction scheme [22] which gives an interaction Hamiltonian of

$$\hat{H}_I(t) = I(t)\hat{\phi} \tag{3.4}$$

where $I(t)$ is the current being driven through the circuit at time t. This is the basic premise behind our photo-detector. At the left in figure 3.1 is a terminal connected across any resonating cavity from which the photon originates; a 1-dimensional wave-guide along which at some point there is coupling to a qubit –perhaps a charge qubit, for example [10].

We define the power flowing out of the transmission [29] line as

$$P = \frac{I(t)^2}{2} Z_0. \tag{3.5}$$

[1] Although the critical current I_c can be altered to change the shape of the potential, this would be primarily for the purpose of altering the height of the potential metastable barrier –a change that can also be accomplished by altering the external biasing ϕ_x. Since I_c is a physical property of the circuit, and ϕ_x is a control parameter (and resonance requirements constrain our metastable-well curvature to a single degree of freedom), we will manipulate the potential via ϕ_x, and assume constant $I_c = 2\mu A$ (a value consistent with experiment [26] [27] [28]) yielding $E_J = 6.58 \times 10^{-22} J$

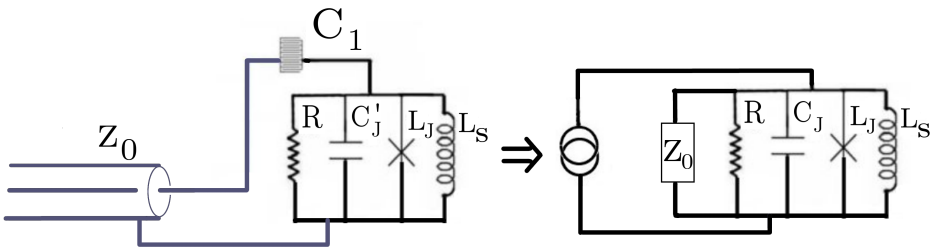

Figure 3.2: Norton equivalency of our detector circuit, where C_J, L_s are the effective capacitances and inductances of the whole circuit, Z_0 is the impedence of the transmission line, and the photon is treated as a current source.

Here Z_0 is the impedence of the transmission line, which, due to geometrical considerations, is approximately $Z_0 = 50\Omega$. We will assume that the resistance of the detector circuit, R, is sufficiently large that negligible power is dissipated into it on the time scale of the photon period $\frac{2\pi}{\omega}$. To be assured of energy conservation, we consider the power emitted from the transmission line (equation 3.5) and apply this relation to equation 3.4 to impose the constraint that

$$\int_{t=-\infty}^{\infty} \frac{I(t)^2}{2} Z_0 \, \mathrm{d}t = \hbar\omega_R, \tag{3.6}$$

where ω_R is the drive frequency of the photon.

Once the current has excited the system, energy is then dissipated from the tank circuit into the environment through the resistor, a process which we model using incoherent state transitions (see chapter 6.) The rate at which this occurs is inversely proportional to the quality factor of the circuit Q, which, for a parallel RLC circuit with resonant frequency ω_0 is given by

$$Q = \frac{R_T}{\omega_0 L}, \tag{3.7}$$

where R_T is the total real impedence of the circuit. To make this quantity more transparent, we construct a Norton equivalent of our circuit, including the transmission line, as shown in figure 3.2. Here it is apparent that the total real resistance is

$$R_T = \frac{RZ_0}{R + Z_0}. \tag{3.8}$$

Given equation 3.8, an upper limit to R_T (and thereby also Q) arises, since $R_T \to Z_0$ in the limit of $R \to \infty$. Assuming $Ls = 266pH$, $\omega_0 = 37Grps$ (these quantities are

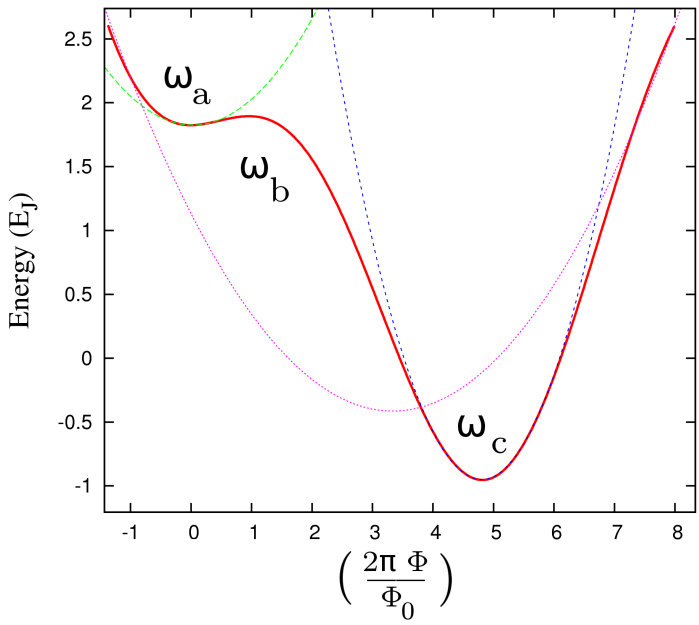

Figure 3.3: The double well, generated in the ϕ dimension, by quadratic, and cosine terms in equation 3.3, and the three harmonic approximations applicable to it. The curvature of these latter wells will be used in analytic estimations of the periodicity of the system, and level separation, as well as its decay rate. Note that the middle frequency ω_b denotes $\sqrt{\frac{V''(q)}{m}}$, at the barrier peak, a characteristic feature of the barrier that will be used in chapter 5

constrained by resonance requirements), and $Z_0 = 50\Omega$ we obtain an upper limit of $Q = 5$ from equation 3.7. Assuming that transmission lines can, in principle, be fabricated with an impedence as high as 100Ω, we can obtain a Q-factor as high as 10, though higher Q values than this do not seem feasible. As it turns out, this constraint is immaterial, since we will observe in chapter 6 an optimal quality factor of approximately 7.

Having explored the delivery mechanism of energy into our detector, we now turn our attention to the energy eigenstates of our circuit.

3.2 Harmonic basis expansion

We have still yet to assign specific numeric values to many of the constants involved in equation 3.3, however, we know that the shape of the potential defined by the ϕ-dependent terms of 3.3 can -with appropriate biasing in the form of ϕ_x- be made to look like an asymmetric, or tilted, double well in flux. Each of these two wells can in turn be approximated by a harmonic well, as shown in figure 3.3.

The energy eigenstates $|\sigma_n\rangle$ to the harmonic well, of course, constitute a well-

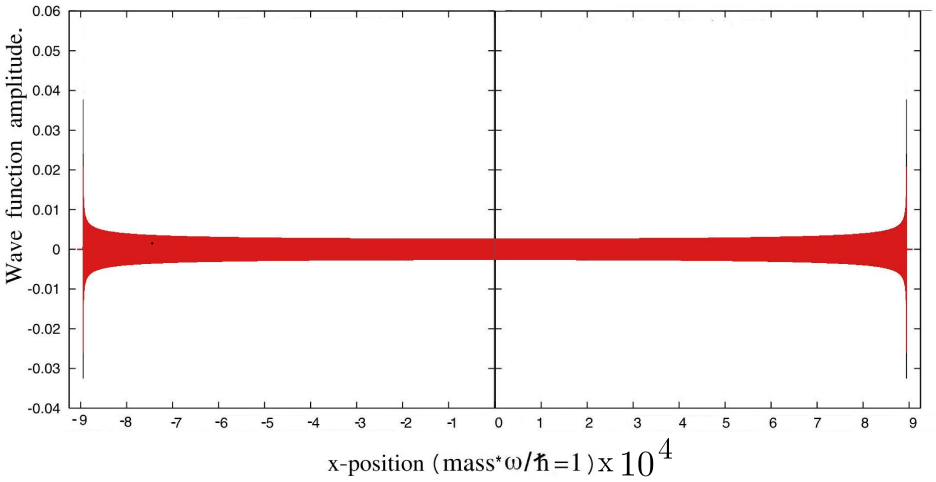

Figure 3.4: The $4 \times 10^9 - th$ eigenstate solution to the harmonic oscillator in units of $x_0 = \sqrt{\frac{\hbar}{m\omega_c}}$. In practise, the reconstruction of our eigenstates requires only a linear combination of eigenstates up to $n \approx 6,000$, but the above plot shows the robustness of our approach.

known and fully analytic set of solutions, given by:

$$\begin{aligned}
\langle\phi|\sigma_n\rangle &= \frac{1}{\sqrt{n!}}\langle\phi|(a^\dagger)^n|0\rangle \\
&= \frac{1}{\sqrt{n!}}\left(\sqrt{\frac{m\omega_c}{2\hbar}}\right)^n\left(\phi - \frac{\hbar}{m\omega_c}\frac{\mathrm{d}}{\mathrm{d}\phi}\right)^n\left(\frac{m\omega_c}{\pi\hbar}\right)^{\frac{1}{4}}\mathrm{e}^{\left[-\mathrm{m}\omega_\mathrm{c}\frac{\phi^2}{2\hbar}\right]} \\
&= \frac{m\omega_c}{\pi\hbar}\frac{1}{\sqrt{2^n n!}}\mathrm{H_n}\left(\sqrt{\frac{\mathrm{m}\omega_\mathrm{c}}{\hbar}}\phi\right)\mathrm{e}^{\left[-\mathrm{m}\omega_\mathrm{c}\frac{\phi^2}{2\hbar}\right]} \qquad (3.9)
\end{aligned}$$

where $\mathrm{H_n(x)}$ represents the n^{th}-order Hermite polynomial of x. Naturally, for large n, direct evaluation of 3.9, becomes intractable; we may still evaluate the position-basis wave function, however, by exponentiating the sum of the logarithms of each factor in 3.9. This method requires asymptotic analysis of the Hermite polynomials -a result which is provided by Dominici [30]. Using this definition of the wave-functions, and manipulating the relevant terms in this way, practically arbitrarily large order solutions to the harmonic well can be generated. Figure 3.4 shows the 4-billionth solution to the harmonic well as a function of position.

While the energetic parabolas serve as a useful approximation to either of the wells in our potential, over the entire range of interest, the double well in figure 3.3 can be approximated by a 4^{th} order polynomial in the position coordinate.

$$V(\hat{\phi}) = \frac{(\hat{\phi} - \phi_x)^2}{2\beta} - \cos(\hat{\phi}) \approx c_1\hat{\phi}^4 + c_2\hat{\phi}^3 + c_3\hat{\phi}^2 + c_4\hat{\phi} + c_5 \qquad (3.10)$$

for c_{1-5} to be determined by least-squares regression. Choosing the harmonic system as a basis, and expressing the potential as in 3.10 allows us to insert the position and momentum operators of the harmonic well

$$\hat{\phi} = \sqrt{\frac{\hbar}{2m\omega_c}}\left(\hat{a} + \hat{a}^\dagger\right) \tag{3.11}$$

$$\hat{q} = -\mathrm{i}\sqrt{\frac{\mathrm{m}\omega_\mathrm{c}\hbar}{2}}\left(\hat{\mathrm{a}} - \hat{\mathrm{a}}^\dagger\right) \tag{3.12}$$

into the polynomial terms of (3.10).

These operators can then be inserted into equation 3.3 which, when diagonalized, produces eigenstates comprised of superpositions of the harmonic states $|\Psi_n\rangle = \sum_i c_i|\sigma_i\rangle$. Provided sufficiently large number of basis states are taken ($\approx$ 6000), the eigenstate solutions generated exhibit localized densities in the valleys of the double well as expected.

3.3 Discrete variable representation

A far more efficient and accurate method exists –as we have found from the work of Colbert et al [17]– in the discrete variable representation (DVR.) This is a preferable method of resolving the position-basis wave-functions of our eigenstates for three reasons. First, the *exact* potential well can be considered, as opposed to harmonic method above, in which a polynomial approximation to the potential must be employed.

If we generate the polynomial coefficients c_{1-5} in equation 3.10 using regression over the whole double well, then our profile of the potential tends to break down as an approximation in the vicinity of the metastable well (precisely the region in which we are most interested in accurately reproducing the potential curvature.) This discrepancy casts the spatial resolution of the energy eigenstates from the harmonic basis expansion in doubt.

Secondly, the number of basis states required to generate our eigenstates using DVR is about $\frac{1}{6}$ the basis set size necessary in the above method. Since the time required for diagonalization scales with the basis size according to a power law, this speeds up our calculations significantly. Finally, the errors associated with both the eigenenergies, and the wave-function profiles scale with a single parameter Δx which we will consider below:

To reproduce the discrete variable representation, we discretize the position dimension into positions with indices ϕ_i. Our position-space Hamiltonian then need not be approximated as in 3.10; we express our Hamiltonian in the form [17]

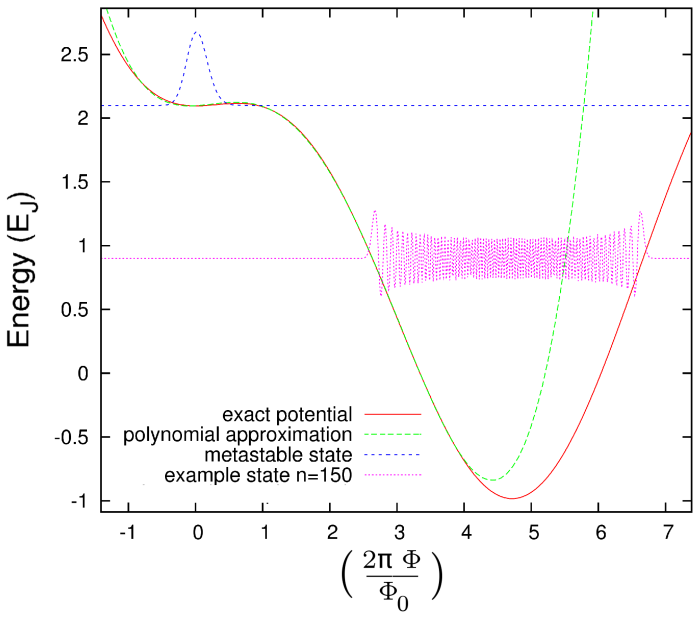

Figure 3.5: The potential well 3.10 alongside its polynomial approximation, with the metastable eigenstate and an example state within the stable well plotted. Note the discrepancies between the approximation and the actual potential – accurate representations of the metastable curvature necessarily entail inaccurate widths of the potential well on the right.

$$\hat{H} = \hat{V} + \hat{T} = \sum_{j,k} |j\rangle\langle k| \left(\delta_{jk} V(\phi_j) + \frac{\hbar^2 (-1)^{j-k}}{2 C_J \Delta x^2} \left\{ \begin{array}{ll} \frac{\pi^2}{3}, & \text{if}(j = k) \\ \frac{2}{(j-k)^2}, & \text{if}(j \neq k) \end{array} \right\} \right). \quad (3.13)$$

In equation 3.13, $\hat{T}$ is the kinetic energy operator expressed as an infinite order finite difference approximation for the second derivative [17] for uniformly spaced positions ϕ_i. This process amounts to taking a basis of states $|\alpha_n\rangle$ that solve the infinite square well over some bounded region of a potential and, through diagonalization, obtaining the energy eigenstates $|\Psi_n\rangle = \sum_k c_k |\alpha_k\rangle$.

The key control variable in this entire process is the external flux, ϕ_x, from equation 3.10, since it determines the asymmetry of the potential. A few examples of the resulting eigenstates using this method are shown in figure 3.5, assuming sufficient external flux to generate a potential well such that the left minimum is separated from the right well by a potential barrier of height $V_B = 0.016 \mathrm{E_J}$ (all data presented in this chapter assume this barrier height; the reason for this choice of potential profile will be explained in chapter 6.)

Using the same set of eigenstates, state energies, E_n, are plotted against their index n in figure 3.6, exhibiting a surprisingly linear dependence on n –in marked similarity to a harmonic system despite the obvious anharmonicities of the potential.

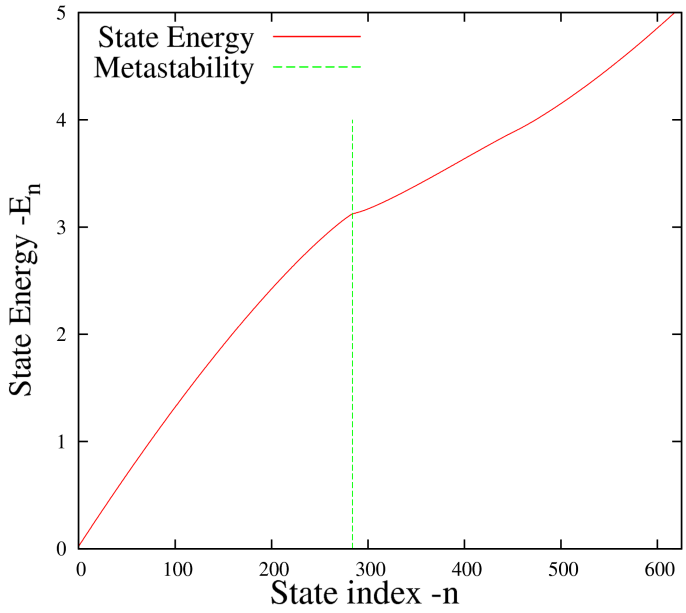

Figure 3.6: Eigen-energies resulting from the solution of 3.13. the metastable barrier generates a change in the slope, but otherwise the energy dependence is very much linear, despite the obvious anharmonicity of the potential shown in figure 3.5.

Furthermore, since our driven Hamiltonian will depend on the coupling strength between each of these eigenstates $\phi_{jk} = \langle j|\hat{\phi}|k\rangle$, we determine these coupling coefficients not by the definition given in 3.11, but by numerical integration

$$\phi_{jk} = \int_{\phi=-\infty}^{\infty} \mathrm{d}\phi \langle\phi|\Psi_\mathrm{j}\rangle \phi \langle\Psi_\mathrm{k}|\phi\rangle \tag{3.14}$$

using the trapezoidal integration rule. Of course, these wave functions are entirely real in the Schrödinger frame, hence we need not concern ourselves with the complex conjugates implied by equation 3.14.

3.4 Coupling coefficients

As we will see in chapter 6, the coefficients of 3.14 play a pivotal role in the time evolution of our system; for computational considerations, however, it is useful for us to restrict the Hilbert space used in this time evolution to states near in energy to the metastable barrier. We justify this truncation by considering the exponential decay of the coupling strengths in equation 3.14 with the energy difference between the given states. To demonstrate this, figure 3.7 shows the coupling strength of each

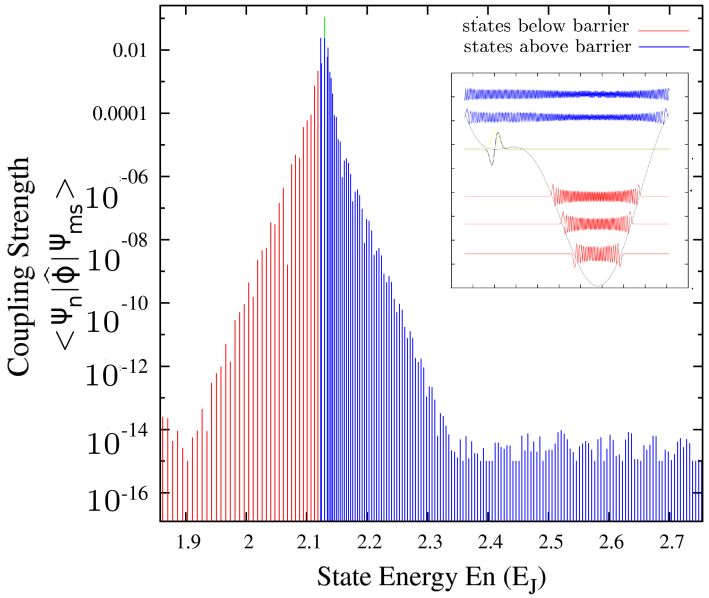

Figure 3.7: coupling strength, $\langle \Psi_n|\hat{\phi}|\Psi_{ms}\rangle$, of each state with the lowest-energy metastable state –which we presume to have unity occupation probability at time $t = 0$. For $V_B = 0.016$, this metastability occurs for state ms=284. The exponential decay is an indication that states very high above the barrier will have negligible probability of direct excitation.

state with the initial state (i.e. the lowest energy state localized to the metastable region) – an exponential decay is evident.

Figure 3.8 shows the coupling strengths, as a function of n, the eigenstate index (indexed such that $E_n \leq E_{n+1} \forall n$), for states and their nearby energy states. It is clear that neighbouring states will dominate the coupling via ϕ; we will see in chapter 6 that this indicates the state will generally make low-energy transitions between neighbouring states until it decays to stability –radiating away its energy gradually in the process.

With these coupling strengths we are able to add great depth to the model introduced in chapter 2, and proceed to more realistic photo-detection models. It is useful, however, to also consider the activation of such a metastable system in a classical model; doing so will allow us to generate analytic predictions of the spontaneous, or dark, rate of the system, as well as driven resonance responses and compare both with our quantum model.

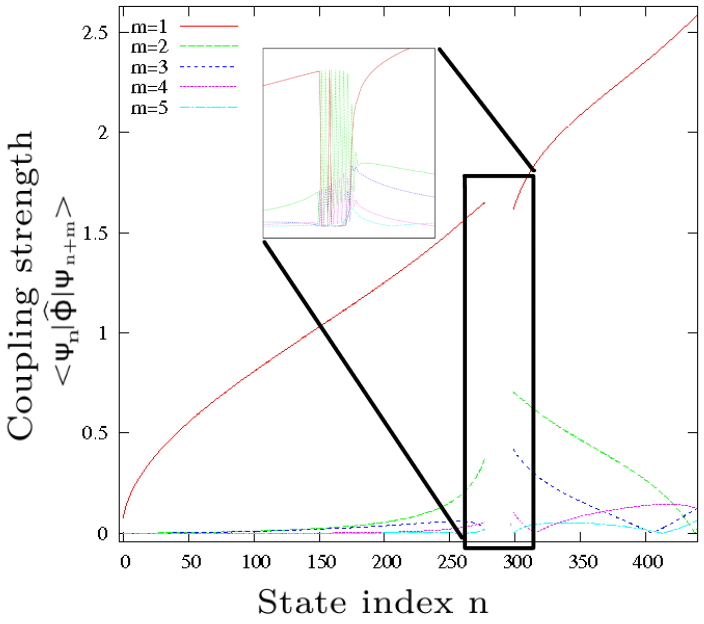

Figure 3.8: Coupling strengths $\langle\Psi_n|\hat{\phi}|\Psi_{n+m}\rangle$. as a function of n for $m = 1 \ldots 5$ for $V_B = 0.016$. Clearly the $\langle\Psi_n|\hat{\phi}|\Psi_{n+1}\rangle$ term dominates, indicating that excitation and decay process are likely to occur along a 'staircase' of adjacent levels.

Chapter 4

Classical activation

Although the bulk of our results and work will stem from the numerical work undertaken in chapter 6, it is always useful to have an analytic approximation as a gauge for comparison. To this end, we study the classical activation rates of metastable systems -first by considering driven anharmonic oscillations of a classical particle in a well[18], and secondly, by exploring the stochastic methods of various authors [19, 31, 20] applied to classical probability distributions in metastable potentials. These approximations, of course, have their shortcomings when applied to the system under consideration; level discretization, finite barrier widths, and tunnelling amplitudes all undermine the applicability of these models to the system of interest. Nevertheless, they elucidate the resonance frequencies of our system for a given potential well, and provide an analytic expression for the escape rate as a function of the barrier height, both of which we will compare against the results of our quantum model in chapter 6.

4.1 Classical anharmonic drive

Consider, as in equation 3.10, a polynomial approximation to our double well $V(q)$ (we will use q to denote position, only throughout this chapter); we begin by defining our system Lagrangian

$$L = \frac{1}{2}m\dot{q}^2 - c_1q^4 - c_2q^3 - c_3q^2 - c_4q - c_5 \tag{4.1}$$

and we apply the classical Euler-Lagrange equations

$$\frac{\partial L}{\partial q} - \frac{\mathrm{d}}{\mathrm{dt}}\left(\frac{\partial L}{\partial \dot{q}}\right) = 0 \tag{4.2}$$

to obtain our equations of motion. We define $\tilde{q} = q - q_0$, where q_0 is the metastable minimum such that $4c_1q_0^3 + 3c_2q_0^2 + 2c_3q_0 + c_4 = 0$, and insert $q = \tilde{q} + q_0$ into our potential to obtain

$$\ddot{\tilde{q}} + \omega_0^2 \tilde{q}(t) = -\alpha \tilde{q}(t)^2 - \beta \tilde{q}^3 \tag{4.3}$$

with above constants defined as follows:

$$\begin{aligned} \omega_0^2 &= \frac{(12c_1 q_0^2 + 6c_2 q_0 + 2c_3)}{m} \\ \alpha &= \frac{12c_1 q_0 + 3c_2}{m} \\ \beta &= \frac{4c_1}{m}. \end{aligned} \tag{4.4}$$

The solution to equation 4.3 can be expressed using perturbation theory; hence, we assume that position as a function of time can be expressed as a perturbative sum $q(t) = q^{(1)}(t) + q^{(2)}(t) + q^{(3)}(t) + \ldots$, and the anharmonic frequency $\omega = \omega_0 + \omega^{(1)} + \omega^{(2)} + \ldots$. Through expansion in an arbitrary, normalized order parameter [1] a, we determine the order terms of the position coordinate

$$\begin{aligned} q^{(1)}(t) &= a\cos(\omega t) \\ q^{(2)}(t) &= \frac{-\alpha a^2}{2\omega_0^2} + \frac{\alpha a^2}{6\omega_0^2}\cos(2\omega t) \\ q^{(3)}(t) &= \frac{a^3}{16\omega_0^2}\left(\frac{\alpha^2}{3\omega_0^2} - \frac{\beta}{2}\right)\cos(2\omega t). \end{aligned} \tag{4.5}$$

While the zeroth order oscillation frequency is given above, the higher order terms are determined to be:

$$\begin{aligned} \omega^{(1)}(t) &= 0 \\ \omega^{(3)}(t) &= a^2\left(\frac{3\beta}{8\omega_0} - \frac{5\alpha^2}{12\omega_0^3}\right). \end{aligned} \tag{4.6}$$

If we insert a driving force into equation 4.3 we obtain the driven equation of motion

$$\ddot{\tilde{q}} + 2\lambda\dot{\tilde{q}} + \omega_0^2\tilde{q}(t) = (f/m)\cos(\omega_R t) - \alpha\tilde{q}^2 - \beta\tilde{q}^3. \tag{4.7}$$

Given (4.7), we consider the dependence of the system dynamics on the driving amplitude f, and frequency ω_R, as shown in figure 4.1. One notices two key aspects of this data: first, an optimum drive frequency is illuminated which is slightly ref-shifted from the from the harmonic approximation of 41 Grad/s to the metastable

[1] the term 'order parameter' here is used in the sense of perturbative expansion, not to be confused with the term 'order parameter' as used in a superconducting electronic context.

well, and secondly, higher-order resonant frequencies appear. According to Landau [18], a resonance point is to be expected for ever drive frequency that satisfies $\omega_R = \frac{j}{k}\omega_0$, where j and k are integers; the two ancillary resonances observed in figure 4.1 appear to be $\frac{1}{2}\omega_0$ and $2\omega_0$ respectively. Both of these characteristics will be reproduced in the results of our quantum mechanical model in chapter 6.

The data shown in figure 4.1 are a scan over the $f-\omega_R$ parameter space assuming $VB = 0.016E_J$ –we will see in chapter 6 why this particular barrier height is significant. Figure 4.2 shows the trajectory of such a particle as a function of time at this barrier height, on resonance with the minimal drive amplitude f necessary to elicit a transition seen at time $t \approx 1$ns followed by dissipative oscillation in the stable well.

One must also ascertain, at what *rate* the particle will relax into the ground state once transition has occurred. To this end, figure 4.3 shows the fraction of energy that is dissipated per cycle as a function of the dissipation constant λ, from equation 4.7. This measure of damping magnitude on energy dissipation will serve as a gauge of validity for dissipation rates used in our quantum model in chapter 6.

Naturally, in any quantum-mechanical system, we cannot restrict our model to point-particles. Hence, in the following section we consider the stochastic differential equations necessary for the time evolution of a realistic open probability distribution in a metastable well.

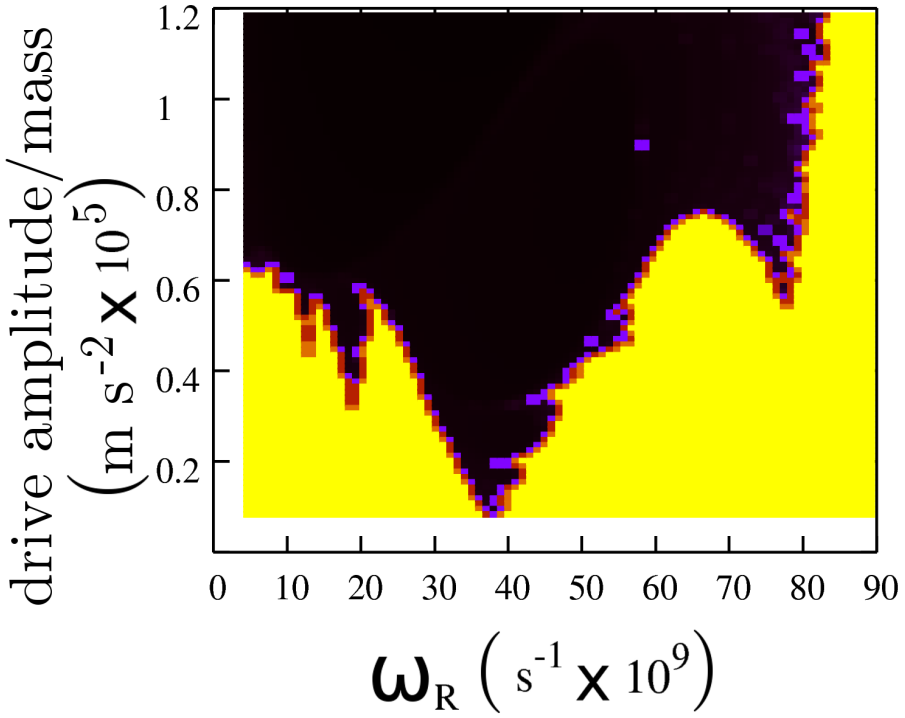

Figure 4.1: Classical activation as a function of the drive frequency and forcing amplitude for a point particle in a double well analogous to the flux bistability with the energetic metastable barrier (henceforth denoted V_B) set to $V_B = 0.016$. The 2-D plane above is in the dimension of drive frequency and amplitude per unit mass (in units of $N/kg \equiv m/s^2$ for such a classical analogy). In the dark-shaded region the particle will transition over the barrier *eventually*, while in the light-shaded region it never will. Note that the local minimums in necessary drive amplitude denote resonances at $\omega = 37, 78$, and 19Grad/s (a minor resonance point as well may be noticed at $\omega = 13$Grad/s,) we will see these same resonance peaks nearly exactly in the quantum model in chapter 6.

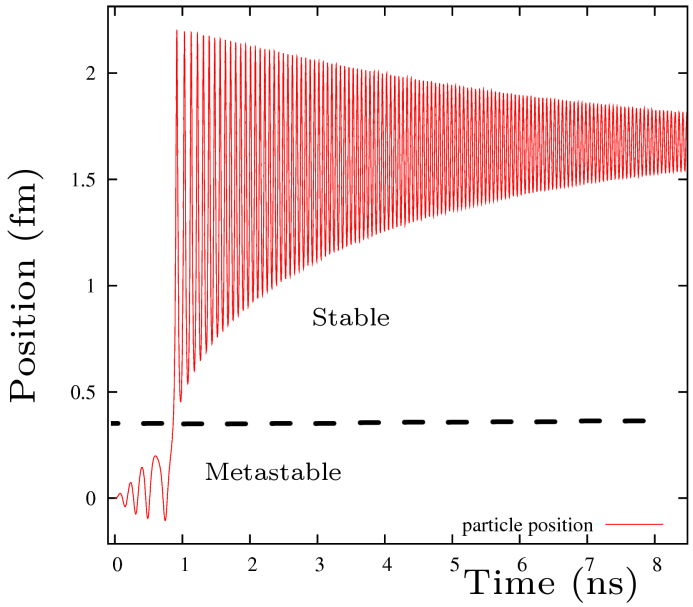

Figure 4.2: Position of a point particle as a function of time with minimal necessary drive amplitude at resonance assuming $V_B = 0.016$. the point of transition from metastability is apparent, after which point the system dissipates energy until it relaxes in the stable position.

4.2 The Langevin treatment

We begin by considering a probability distribution spread through a metastable potential well, as in the metastable state shown in figure 3.5. We presume the right, or stable, well to be sufficiently deep to prevent return, and treat entry into this well as an absorbing boundary conditions. We consider a particle somewhere in this distribution, and use its equations of motion to derive the full Fokker-Planck differential equation describing the evolution of the probability distribution associated with it. The deterministic differential equations describing the motion of a particle in this potential, with zero forcing, are given by 4.8.

$$\ddot{q} + \gamma\dot{q} + K(q) = 0 \tag{4.8}$$

where γ represents the damping of the system divided by it's mass and $K(q) = \frac{U'(q)}{m}$ is the first derivative of the potential divided by mass. Considering the scaled dimensions of equation 4.8 (where $m = 1$) we can set the momentum of the system $p = \dot{q}$ in order to reduce the 2^{nd} order differential equation to a first order problem. Applying these relations to equation 4.8 we see that

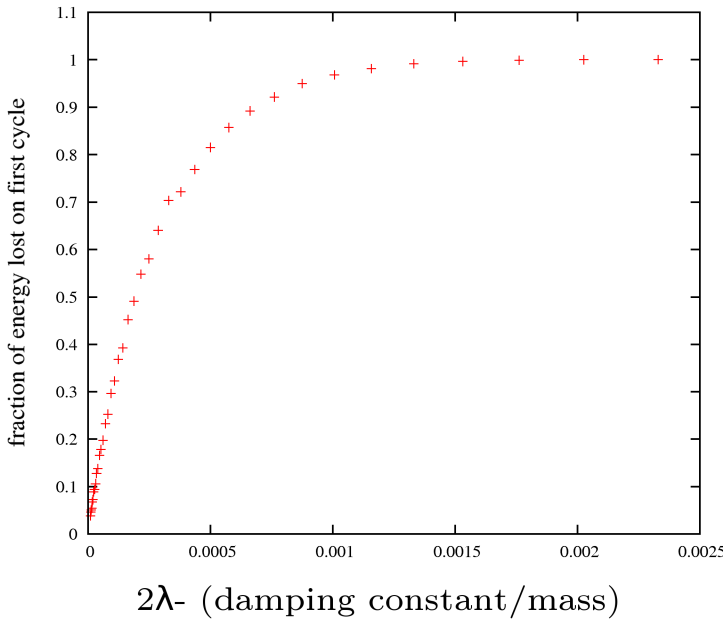

Figure 4.3: Energy fraction dissipated per unit cycle as a function of the dissipation constant divided by mass –2λ in equation 4.7. This quantity will guide our selection of desired quality factor, since we will ultimately desire a system with sufficiently fast dissipation to relax the state once transition has occurred, but not so rapidly as to dissipate energy before then.

$$\dot{q} = p \tag{4.9}$$
$$\dot{p} = -K(q) - \gamma p. \tag{4.10}$$

We now consider an arbitrary function $f(p,q)$ and its average time derivative

$$\frac{d}{dt}\langle f(p,q)\rangle = \left\langle \frac{df(p,q)}{dt} \right\rangle. \tag{4.11}$$

Here the brackets $\langle\rangle$ denote time-averages over the time scale of one period $\frac{2\pi}{\omega_0}$. We can still, however, compute its change in time dt, over longer time scales

$$d\,\langle f(p,q)\rangle = \langle d\, f(p,q)\rangle\,. \tag{4.12}$$

The left hand side of equation 4.12 can be written as:

$$LHS = \frac{d}{dt}\iint_{-\infty}^{\infty} dpdq f(p,q) W(p,q,t) \tag{4.13}$$

where $W(p,q,t)$ is the probability density, or weighting as a function of p and q. The right hand side of equation 4.12 can be written as

$$\begin{aligned} RHS &= \iint_{-\infty}^{\infty} dp\,dq \left[\frac{\partial f(p,q)}{\partial q}\left(\frac{dq}{dt}\right)\,dt + \frac{\partial f(p,q)}{\partial p}\left(\frac{dp}{dt}\right)\,dt + \mathcal{O}(dt^2)\right] W(p,q,t) \\ &= \iint_{-\infty}^{\infty} dp\,dq \left[p\frac{\partial f(p,q)}{\partial q}\,dt + (-K(q)-\gamma p)\,\frac{\partial f(p,q)}{\partial p}\,dt + \mathcal{O}(dt^2)\right] W(p,q,t) \end{aligned} \tag{4.14}$$

(where we have Taylor expanded $f(p,q)$, keeping only terms which are first order in dt.)

Given equations 4.13 and 4.14, we proceed along a derivation outlined in appendix A to obtain the time evolution of the weighting function assuming no thermal disturbances to the system:

$$\frac{\partial}{\partial t}W(p,q,t) = -p\,\frac{\partial W(p,q,t)}{\partial q} + K(q)\frac{\partial W(p,q,t)}{\partial p} + \gamma\,\frac{\partial\left(p\,W(p,q,t)\right)}{\partial p}. \tag{4.15}$$

Equation 4.15 gives us the Fokker-Planck equation for the above problem. Of course, thermal effects are central to our evaluation of dark currents, and hence we

return to relations 4.8 - 4.10 and introduce stochastic driving. We accomplish this by defining a Gaussian random variable w (lower-case w to distinguish this variable from the probability density W above) with zero mean, such that

$$\frac{d}{dt}w = \xi(t) \tag{4.16}$$

where $\xi(t)$ is a stochastic function of t. Hence, we adapt the relations given in 4.10 to account for the above effects:

$$\begin{aligned} \dot{q} &= p \\ \dot{p} &= -K(q) - \gamma p + \sqrt{N}\xi(t) = -K(q) - \gamma p + \sqrt{N}\frac{dw}{dt}. \end{aligned} \tag{4.17}$$

As with equations 4.13 4.14, we again we proceed from this partial differential equation to determine the dynamics of the diffusion of the weighting function (again, see appendix A), this time with drive incorporated explicitly:

$$\frac{\partial}{\partial t}W(p,q,t) = K(q)\frac{\partial W(p,q,t)}{\partial p} - p\,\frac{\partial W(p,q,t)}{\partial q} + \frac{\partial}{\partial p}\left(\gamma\, p\, W(p,q,t) + \frac{N}{2}\frac{\partial W(p,q,t)}{\partial p}\right). \tag{4.18}$$

Equation 4.18 is the Kramer's equation with stochastic driving; it is the foundation for the diffusion rates which we will determine throughout the remainder of this chapter.

4.3 The small damping limit

We consider an anharmonic potential well with two local minima as shown in figure 4.4

Assuming the noise and damping effects on the system are sufficiently small, we assume that energy is approximately conserved on the time scale of one oscillation (this is the *energy-diffusion* regime.) For a given energy then, the particle will trace out a characteristic path in phase-space. A probability distribution of particles along different phases (for a symmetric potential well, unlike figure 4.4) in this oscillation is shown in figure 4.5 [19].

The non-uniformity shown by the localized 'clump' at the bottom-right in figure 4.5 is reflective of the fact that the distribution - at least initially - could move as a cluster throughout phase space. For this reason, it is convenient to take an average of $W(p,q,t)$ over this closed loop, or equivalently, at a given point p,q averaged over one period in time. Since the trajectory in phase space is characteristic of the

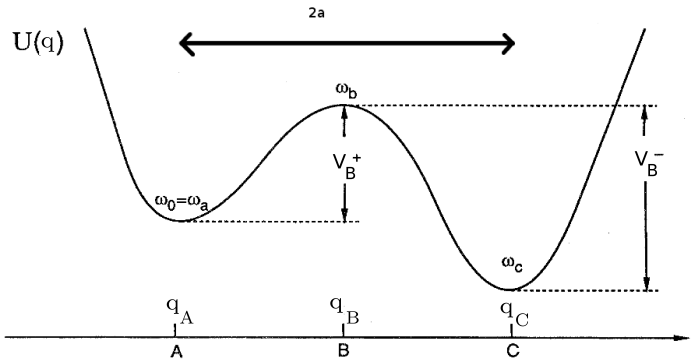

Figure 4.4: A potential well with two local minima in which a particle will oscillate with -initially- enough energy to surmount the barrier in between. We assume that dissipative forces are sufficiently weak that the change in energy of the system upon completion of one period is small. Image adapted from Hänggi et al [19]

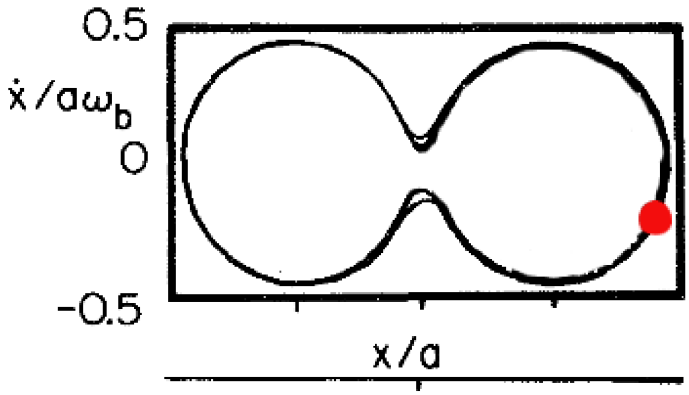

Figure 4.5: The domain, in phase space, occupied by the probability distribution of a particle with a given energy at a snapshot in time. Note the non-uniformity (digitally added) demonstrated by the high density packet near the bottom right. As time goes on, this packet will travel along the trajectory traced out clock-wise, eventually returning (approximately) to its starting point. Image adapted from Hänggi et al [19].

particle's energy, we can define such an average in terms of energy and time in two ways.

$$\rho(E,t) = \oint W(p,q,t)dI = \iint_{-\infty}^{\infty} dp\,dq\ \ \delta\left(E - E'(p,q)\right) W(p,q,t) \tag{4.19}$$

where T is the period of oscillation, I is the area circumscribed by the phase-space path, and dI is the area of a loop, or trajectory, in phase space. Applying this definition to 4.18 we can take γ and N to be arbitrarily small; in the limit $\gamma, N \rightarrow 0$ the energy of the system will not change, hence, the area within the phase space path should remain constant, therefore:

$$\frac{d}{dt}\rho(E,t) = K(q)\frac{\partial\rho(p,q)}{\partial E}\frac{dE}{dt} - p\,\frac{\partial\rho(E,t)}{\partial E}\frac{dE}{dq} = 0. \tag{4.20}$$

That is to say, the distribution will migrate neither outward nor inward, hence, if we are concerned only with the change in energy of the distribution with time, the first two terms of 4.18 can be neglected.

For the remaining term, we note that

$$\begin{aligned}
\overline{\frac{\partial}{\partial p}\left(\gamma\, p\, W(p,q,t) + \frac{N}{2}\frac{\partial W(p,q,t)}{\partial p}\right)} &= \frac{\partial}{\partial p}\left(\gamma\, p\,\rho(E,t) + \frac{N}{2}\frac{\partial\rho(E,t)}{\partial E}\frac{dE}{dp}\right) \\
&= \gamma\left(\rho + \overline{p^2}\frac{d\rho}{dE}\right) + \frac{N}{2}\left(\frac{\partial\rho(E,t)}{\partial E} + \overline{p^2}\frac{\partial^2\rho(E,t)}{\partial E^2}\right) \\
&= \left(1 + \overline{p^2}\frac{\partial}{\partial E}\right)\left(\gamma\rho + \frac{N}{2}\frac{\partial\rho}{\partial E}\right).
\end{aligned} \tag{4.21}$$

If we now exploit the relations $\overline{p^2} = I\omega$, and $\omega = \frac{dE}{dI}$, and simplify expression 4.21 we obtain:

$$\frac{\partial\rho}{\partial t} = \frac{\partial}{\partial I}\left(I\gamma\rho + \frac{N}{2}I\frac{\partial\rho}{\partial I}\right) \tag{4.22}$$

This is the diffusion relation along the action, or equivalently, energy dimension. As the distribution spreads further, we can calculate the fraction of the distribution that accumulates sufficient energy to surmount the barrier by seeing if the phase-space trajectory crosses the threshold of the potential's local maxima. At this point, we employ a steady-state analysis. We assume that some arbitrary outside source is injecting additional probability to the system in the metastable well, and that particle-probability distribution is destroyed and removed from the system upon transition over the barrier. At steady state then, the addition and removal

of probability from the system should reach equilibrium for a given current J of probability across the barrier.

In order to do this, it is convenient to convert from derivatives with respect to E in 4.22 to derivatives with respect to the action I, keeping in mind that:

$$\frac{\partial E}{\partial I} = \frac{\omega(I)}{2\pi}. \tag{4.23}$$

Hence, we express 4.22 as

$$\frac{\partial}{\partial I}\left(I\gamma\rho + \frac{2\pi N}{2\omega(I)} I\frac{\partial \rho}{\partial I} + J\right) = 0; \quad \frac{\partial \rho(I,E)}{\partial t} = 0. \tag{4.24}$$

Here we have mapped our density equation from functions of position to functions of action or energy. We assume that particles start with zero action, or minimal energy and diffuse upward from thermal activation until they reach a threshold energy V_B, or action I_B at which point they immediately escape. In this case, the distribution remains constant, The situation is analogous to (an oddly shaped) water container with a hose feeding into it at the bottom, spilling out over the top with various -but constant- amounts of water at any given height in between; we seek to determine the rate of flow in from the hose. Note, this effectively implies that the well to the right in figure 4.4 is so deep that particles falling into it never return –a reasonable approximation given the large disparity in well depths of our system.

If we define N as $2\gamma k_B T$, then 4.24 becomes equivalent to the steady-state expression of equation 4.12 in Hänggi *et al*[19]. As formulated by Kramer [20], the metastable escape rate is found to be

$$k = \frac{\gamma I_B}{k_B T}\frac{\omega_0}{2\pi} \mathrm{e}^{\left[-\frac{\mathrm{V_B}}{\mathrm{k_B T}}\right]}. \tag{4.25}$$

Additional details of the above derivation are provided in appendix B.

4.4 The metastable action

We now seek to define the action I_B when the energy is *just* at the cusp of transitioning over the barrier, but remains trapped in the metastable well. To accomplish this we note that the action, in general, is defined as

$$I = \oint p\, dq \tag{4.26}$$

where p is the particle momentum, and q the particle position. We use the potential approximation given in 3.10 (again, replacing $\hat{\phi}$ with q) with one small notational change: we replace ϕ_x with $(\pi + \delta)$, that is to say:

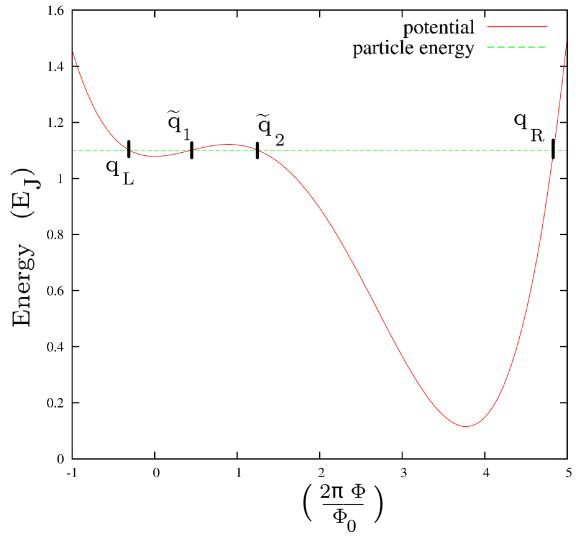

Figure 4.6: Energy of a metastable particle against the quartic approximation to the tilted bistability of figure 4.4. The total energy of the state E minus the potential energy yields, at most, 4 roots –points of physical significance in our model. The roots of equation 4.28 are indicated.

$$U(q) = \frac{(q-(\pi+\delta))^2}{2\beta} - \cos(q) \approx c_0 q^4 + c_1 q^3 + c_2 q^2 + c_3 q + c_4. \tag{4.27}$$

This change in notation in 4.27 -isolating the factor δ- is to highlight the fact that δ represents the degree of 'tilting' introduced to the bistability –when $\delta = 0$ the bistability is perfectly symmetric. We express the action of a particle with energy E as:

$$\begin{aligned} I &= \oint p\,dq = 2\int \sqrt{2m\,(E-U(q))} \\ &= 2\int_{q_L}^{\tilde{q}_1} \sqrt{2m\,(E - c_0q^4 - c_1q^3 - c_2q^2 - c_3q - c_4)} \\ &= 2\sqrt{-2mc_0}\int \sqrt{(q-q_L)\,(q-\tilde{q}_1)(x-\tilde{q}_2)(q-q_R)} \end{aligned} \tag{4.28}$$

where q_L and q_R are the left and right-most roots respectively, and $\tilde{q}_{1,2}$ are the intermediate roots of the state-energy-potential difference, as shown in figure 4.6.

We, however, are concerned with the action *just* at the cusp of the energy level of the barrier, that is, where $\tilde{q}_1$ and $\tilde{q}_2$ become coincident. Equation 4.28 then becomes

$$I_B = 2\sqrt{-2mc_0}\int_{q_L}^{\tilde{q}} \sqrt{(q-q_L)\,(q-q_R)}(q-\tilde{q})$$
$$= 2\sqrt{-2mc_0}\int_{q_L}^{\tilde{q}} \sqrt{(q^2-(q_L+q_R)q+q_Lq_R)}(q-\tilde{q}). \tag{4.29}$$

However, referring to tabled integrals [32] (pg. 99) we see that if we define $R = a + bq + cq^2$ and $\Delta = 4ac - b^2$ then we have the following identities:

$$\int \sqrt{R}\,dq = \frac{(2cq+b)\sqrt{R}}{4c} + \frac{\Delta}{8c}\int \frac{dq}{\sqrt{R}} \tag{4.30}$$
$$\int q\sqrt{R}\,dq = \frac{\sqrt{R^3}}{3c} - \frac{(2cq+b)b}{8c^2}\sqrt{R} - \frac{b\Delta}{16c^2}\int \frac{dq}{\sqrt{R}} \tag{4.31}$$
$$\int \frac{dq}{\sqrt{R}} = \frac{1}{\sqrt{c}}\ln\left(2\sqrt{cR}+2cq+b\right) \tag{4.32}$$

assuming $c > 0$. We now apply these relations to equation 4.29 with the parameters in R and Δ defined as: $a = q_Lq_R$, $b = q_L + q_R, c = 1$. Using these relations (and mathematical software) we arrive at

$$I_B = \frac{c_0 m\tilde{q}\left(\left(\sqrt{\frac{(q_L-q_R)(q_R-\tilde{q})}{q_L-\tilde{q}}} - 2\sqrt{\frac{(q_L-\tilde{q})(q_R-\tilde{q})}{q_L-q_R}}\right)(q_l-\tilde{q}) + (q_L+q_R)^{\frac{3}{2}}\sin^{-1}\left[\frac{1}{\sqrt{\frac{q_L-q_R}{q_L-\tilde{q}}}}\right]\right)}{\sqrt{2}\sqrt{\frac{-c_0m}{q_L-q_R}}}$$

$$-\frac{\sqrt{c_0m}}{6\sqrt{2}}\left((q_L-\tilde{q})\sqrt{\frac{\tilde{q}-q_R}{q_L-\tilde{q}}}\left(3q_L^2-2q_Lq_R+3q_R^2+2q_L\tilde{q}+2q_R\tilde{q}-8\tilde{q}^2\right)+\right.$$
$$\left.3(q_L-q_R)^2(q_L+q_R)\sin^{-1}\left[\sqrt{\frac{q_L-\tilde{q}}{q_L-q_R}}\right]\right). \tag{4.33}$$

Equation 4.33 may seem a bit cumbersome, and practical estimates for I_B may be more easily obtained by applying numerical techniques to equation 4.26. Nevertheless, this analytic result serves as a useful benchmark to validate these numerical results. Over the range of barrier heights which we are concerned with, we note agreement between these two methods of calculating the metastable action. Naturally, the cusp action decreases as δ is increased, since the metastable well shrinks

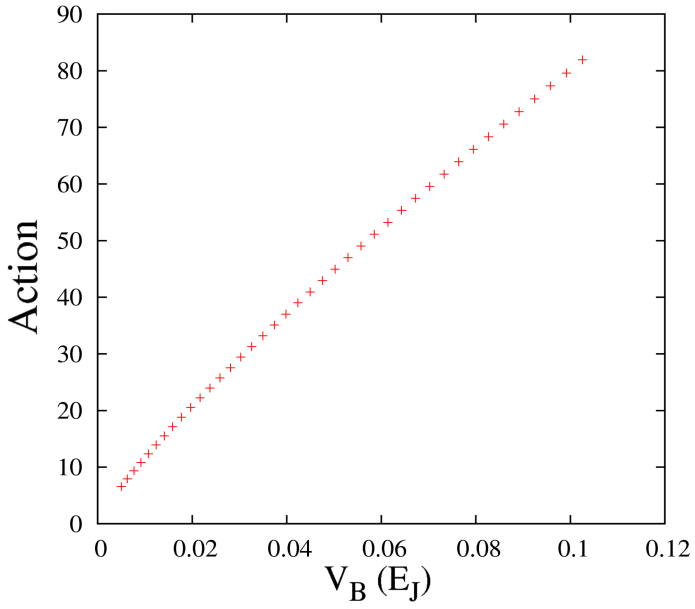

Figure 4.7: The cusp action over the metastable range as a function of barrier height, V_B in units of the Josephson energy (E_J), the relationship is essentially linear.

with increasing asymmetry, and decreasing V_B; the dependence of action on barrier height V_B is determined numerically, and is shown in figure 4.7. Evidently the harmonic approximation of a linear relationship between these two variables is quite reasonable.

4.5 Escape rate results

We now return to the definition of k in equation 4.25, and see how the time-evolution of the probability distribution can be controlled by the parameters used in this derivation. The harmonic frequency ω_0 is defined as:

$$\omega_0 = \sqrt{\frac{1}{m}\left[\frac{\partial^2 U(q)}{\partial q^2}\right]_{q=q_A}}. \tag{4.34}$$

Using this harmonic approximation, we express the quality factor of the metastable well Q, as

$$Q = \frac{\omega_c}{\gamma}. \tag{4.35}$$

Here we use the curvature of the stable well (on the right) to define Q since

it is more consistent across different barrier heights V_B.[2] Furthermore, neglecting backwards reaction into the metastable position, the metastable probability, as a function of time is given by

$$\rho(t) = \mathrm{e}^{[-\mathrm{kt}]} \tag{4.36}$$

and the mean transition time $\langle T \rangle$ of the particle to go over the barrier is then given by

$$\langle T \rangle = \int_0^\infty t\, \mathrm{e}^{[-\mathrm{kt}]}\, \mathrm{dt}. \tag{4.37}$$

$$= \frac{1}{k} \tag{4.38}$$

We assume, provisionally, that $\delta = 0.63$, since this happens to be the value necessary to ensure that only one quantum state is strongly localized in the metastable range. With this value of δ, the barrier height is $V_B = 0.01364 E_J$, the action is $I_B = 15.8$, and the metastable harmonic frequency is $\omega_0 = 40\mathrm{Grad/s}$, with an effective mass of $C_J = 1pF$. The mean life time, for various Q is plotted against temperature in figure 4.8. Unfortunately, with a potential such as this, the spontaneous transition times may be too short to be useful for a practical standing photo-detector. Hence, we attempt to raise the metastable barrier in order to increase the mean life time; the resulting mean life time will determine whether our detection will be useful as a standing detector, or whether a 'pulse protocol' will be necessary to detect photons only for a specific time-intervals of sensitivity. In the latter case, we may simply lower the barrier (by changing δ via ϕ_x) to a specific height that amounts to the optimal trade-off between true-positive detection, and false-positive avoidance.

For example, experiments have found that keeping the system stable over the desirable time scales requires reducing the external biasing such that *six* metastable states are confined to the metastable region [27, 28] with $V_B = 0.05\mathrm{E_J}$. With this arrangement, the increased barrier height significantly reduces the escape rate, as shown by the time scales of figure 4.9. As we will see in chapter 6, a barrier height of this magnitude unfortunately prevents accurate detection when a photon is indeed present; hence, some intermediary value will become a necessary compromise. It turns out that this ideal compromise is reached at $V_B = 0.016\mathrm{E_J}$, for reasons which we will explore in chapter 6; figure 4.10 shows a plot of the mean transition time as a function of T, and Q with this potential.

[2] That is to say: by changing the bias flux ϕ_x, we alter both curvature of the metastable well *and* the barrier height, thus changing ω_0. We therefore use ω_c to define Q, to provide consistent quality factors to compare between various different levels of biasing, since ω_c changes very little over the range of ϕ_x we are concerned with.

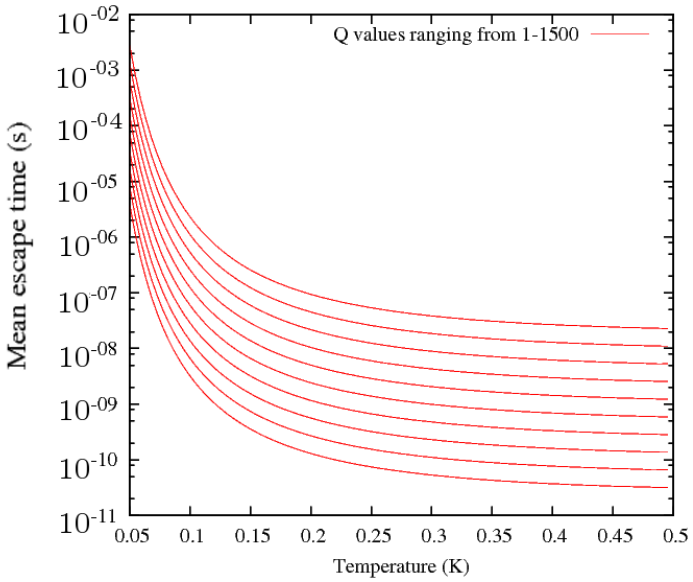

Figure 4.8: Mean transition time as a function of the thermal energy T, for various values of Q between 10 and 1000 for the Martinis qubit system (i.e. with $I_c = 2\mu A$, $C_J = 1pF$, $L_s = 720pH$, $\delta = 2.75$, $V_B = 0.01416E_J$, $I_B = 15.76$ -sufficient metastability to yield only a single quantum state residing in the metastable well.) These time scales are sufficiently short that we must conclude standing photo-detection at 0.1K with this arrangement is not possible.

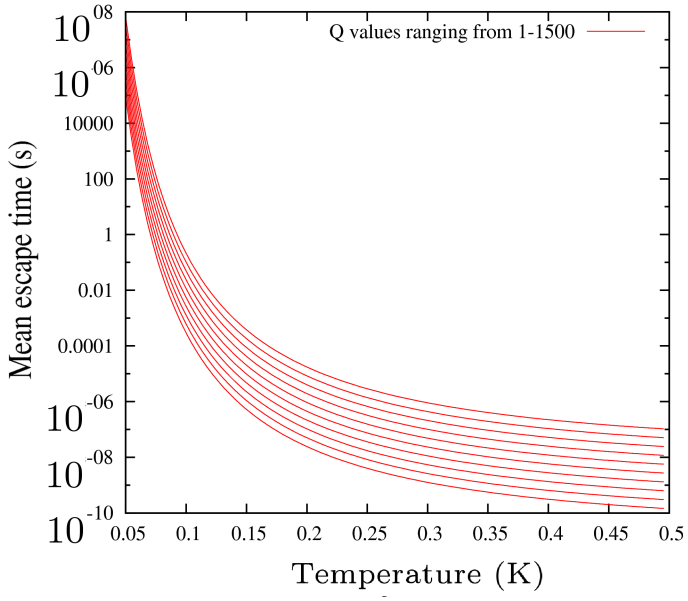

Figure 4.9: mean transition time as a function of the thermal energy T, for various values of Q between 10 and 1000 for the Martinis qubit system, (with $I_c = 2\mu A$, $C_J = 1pF$, $L_s = 720pH$, $V_B = 0.045E_J$, $I_B = 15.76$. except now with asymmetry characterized by $\delta = 2.56$ -sufficient metastability to yield six distinct quantum states localized within the metastable well.) This arrangement has much more potential to be stable on the necessary time-scales for standing photodetection, but may not exhibit sufficient sensitivity.

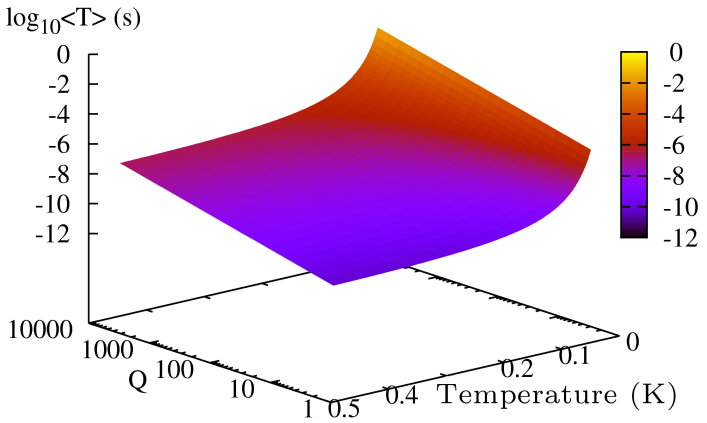

Figure 4.10: Mean transition time, in [log(seconds)], as a function of the ambient temperature T, and the Quality factor Q.

All of the preceding naturally presumes the small damping limit applied to our system, which turns out to be the case. Hence, we need not concern ourselves with the limiting case of large damping, or the *spatial-diffusion limited regime* ; the above limit will suffice.

Chapter 5

The IM-F method

The imaginary part of the Helmholtz free energy holds special significance for metastable system, as an indicator of escape rate. To see this, we employ a number of calculations on this quantity; first we take a thermal average of the tunnelling rates, and use basic statistical mechanics to show how transmission is related to this quantity. Second, we introduce the Euclidean action and perform path integrals through imaginary time over stationary paths in the action. Although our calculation of dark escape rates assumes a more computational approach, the following should be considered valid for very low Q-factor resonators, in which the system reaches thermal equilibrium effectively instantly.

5.1 Thermally averaged tunnelling rates

We begin with a thermal average over the quantum tunnelling rates out of a metastable well, taking temperature into account, but not specifically dissipative dynamics. In the following section, we extend this methodology to dissipative processes by calculating the partition function, Z, using another method developed by Ingold [33, 34].

From statistical mechanics, it is known that the partition function of an ensemble is given by

$$Z = \sum_{n} \mathrm{e}^{[-\beta \mathrm{E_n}]} \tag{5.1}$$

where E_n is the energy of state n, and $\beta = \frac{1}{k_B T}$, assuming E_0 is the system ground state. The situation becomes more complex –in both the literal and mathematical senses– when one considers a metastable ensemble where $n = 0$ no longer corresponds to the ground state of the system, as shown in figure 5.1.

Here, $q_A = 0$ corresponds to a local minimum at the origin and q_b is a local maximum to the right. Furthermore, we define the following frequencies:

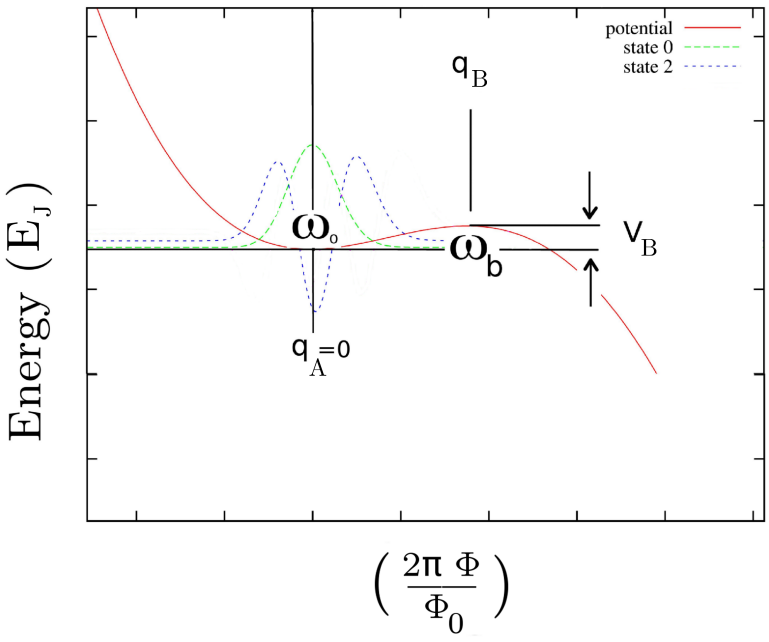

Figure 5.1: A schematic of the potential well $V(q)$ (which can be treated as approximately cubic in q) confining a number of quantum states. We assign ω_0^2 and ω_b^2 to the curvatures of the potential at its extrema divided by system mass at the points $q_A = 0$, and $q = q_B$ respectively.

$$\omega_0 = \sqrt{V''(0)/m} \qquad\qquad \omega_b = \sqrt{V''(q_b)/m}. \tag{5.2}$$

One may note a certain ambiguity associated with the definition of energies in this context; the energies E_n given in equation 5.1 are defined relative to the ground state, but the potential in figure 5.1 is not bounded, and the energy of the states illustrated can only be defined relative to the metastable bottom. To account for this we assign complex values to the eigen-energies E_n; in doing so, with time evolution taking the form $\mathrm{e}^{[-\mathrm{iE_nt}]}$, exponential decay can be accounted for as well as the usual rotations in phase space that are associated with real eigenenergies. Hence, we reformulate our partition function as

$$Z = \sum_n \mathrm{e}^{[-\beta(\mathrm{E_n} - \mathrm{i}\hbar\Gamma_\mathrm{n}/2)]} \tag{5.3}$$

where the parameter Γ_n will be determined shortly. Furthermore, if we assume dense levels, i.e., that $V_B \gg \hbar\omega_0$ then it follows that $\hbar\Gamma_n \ll E_n$ for all n. Thus for large barriers we can Taylor expand about parameter $\frac{i\hbar\beta\Gamma_n}{2}$ taking only the zeroth and first order term. Equation 5.3 then becomes

$$Z = Z_0 + iZ_b \approx \sum_n \mathrm{e}^{[-\beta\mathrm{E_n}]} + \mathrm{i}\frac{\hbar\beta}{2}\sum_\mathrm{n}\Gamma_\mathrm{n}\mathrm{e}^{[-\beta\mathrm{E_n}]}. \tag{5.4}$$

Here the real part is determined by the properties of the well, and the imaginary part is determined by the properties of the barrier. Recall that the free energy is given by

$$F = \frac{-1}{\beta}\ln Z. \tag{5.5}$$

Also recall that for small x, $ln(1+x) \approx x$, hence

$$\begin{aligned} F = \frac{1}{\beta}\ln\left(Z_0 + iZ_b\right) &= \frac{1}{\beta}\ln\left(Z_0\left(1 + i\frac{Z_b}{Z_0}\right)\right) && (5.6)\\ &= \frac{1}{\beta}\left(\ln Z_0 + ln\left(1 + i\frac{Z_b}{Z_0}\right)\right) && (5.7)\\ &\approx \frac{1}{\beta}\ln Z_0 + i\frac{1}{\beta}\frac{Z_b}{Z_0} && (5.8)\end{aligned}$$

provided $|Z_b| \ll |Z_0|$. The thermal quantum escape rate 'k' is related to the imaginary part of the free energy by

$$k = -\frac{2}{\hbar}\mathrm{Im}\left\{\mathrm{F}\right\}. \tag{5.9}$$

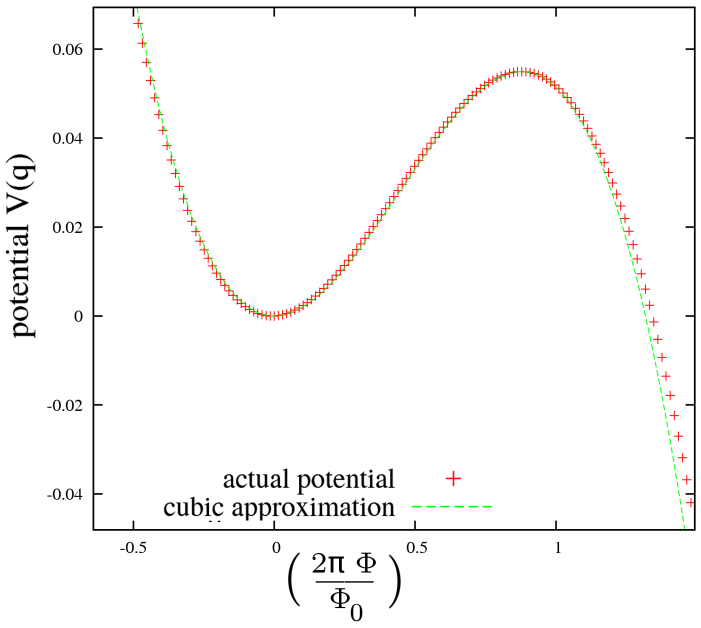

Figure 5.2: Cubic approximation to the potential well in the region of interest.

This relation becomes apparent when one considers applying the time-evolution operator to states with such energy. Using the real and imaginary components of relation 5.8, we find that

$$k = \frac{\sum_n \Gamma_n e^{[-\beta E_n]}}{\sum_n \exp^{-\beta E_n}}. \tag{5.10}$$

Note that this expression for the escape rate is valid only if the distribution within the well-levels is well thermalized; i.e. that the T_1 relaxation time is much shorter than the escape time. All that remains now is to determine the quantum tunneling escape rate for each energy level, i.e. the coefficients Γ_n. It turns out that the regular (*non*-inverted) potential can be approximated by a cubic of the form:

$$V(q) \approx \frac{1}{2} m\omega_0^2 q^2 \left(1 - \frac{2q}{3q_b}\right). \tag{5.11}$$

The validity of this approximation is demonstrated in figure 5.2.

then Γ_0 is the tunneling rate of the ground state, given by WKB analysis as:

$$\Gamma_0 = \omega_0 C_0 \sqrt{\frac{S_0}{2\pi\hbar}} e^{[-S_0/\hbar]}. \tag{5.12}$$

Here C_0 is a numerical factor which depends on the shape of the barrier, S_0 is the bounce action in the inverted potential at zero energy

$$S_0 = I(V_B) = 2 \oint dq \sqrt{2mV_{inv}(q)}, \tag{5.13}$$

and the tunnelling rates of the excited states are again given by WKB analysis as [35]

$$\Gamma_n = \frac{1}{n!} \left(C_0^2 \frac{S_0}{\hbar} \right)^n \Gamma_0. \tag{5.14}$$

Note that for the cubic potential described above, we find $C_0 = \sqrt{60}$, and $S_0 = \frac{6}{5} m\omega_0 q_b^2$, and the barrier height is given as

$$V_b = m\omega_0^2 q_b^2/6 \qquad , \qquad \omega_0 = \omega_b. \tag{5.15}$$

5.2 Bath and system dynamics in damping mechanisms

The partition function, equation 5.3, can also be expressed in another way. To see how this can be done, while incorporating dissipation into a bath coupled to the system, we consider the action of a particle in a well with potential $V(q)$ and mass M over time s from $s = 0$ to time $s = t$.

$$S[q,t] = \int_0^t ds \left(\frac{M}{2} \left(\frac{\mathrm{d}q(s)}{\mathrm{d}s} \right)^2 - V(q(s)) \right). \tag{5.16}$$

We now perform a Wick rotation on the time variable by making the substitutions $t \to -i\hbar\beta$, and $s \to -i\tau$ yielding the Euclidean action $S^E[q, \hbar\beta]$

$$S^E[q,\hbar\beta] = S[q,-\mathrm{i}\hbar\beta] = \mathrm{i} \int_0^{\hbar\beta} \mathrm{d}\tau \left(\frac{\mathrm{M}}{2} \left(\frac{\mathrm{dq}(\tau)}{\mathrm{d}\tau} \right)^2 + \mathrm{V}(\mathrm{q}(\tau)) \right). \tag{5.17}$$

The utility of this rather unintuitive step lies in it's application to a system's equilibrium density matrix, given by

$$\langle q'' | \rho_\beta | q' \rangle = Z^{-1} \int_{q(0)=q'}^{q(\hbar\beta)=q''} Dq \mathrm{e}^{\left[-\mathrm{S^E[q]}/\hbar\right]} \tag{5.18}$$

For an arbitrary ensemble of systems. Naturally, the partition function Z is then

$$Z = \int_{-\infty}^{\infty} \mathrm{dq}\langle \mathrm{q}|\rho_\beta|\mathrm{q}\rangle = \oint_{\mathrm{q}(0)=\mathrm{q}'}^{\mathrm{q}(\hbar\beta)=\mathrm{q}'} \mathrm{Dq} \mathrm{e}^{\left[-\mathrm{S}^{\mathrm{E}}[\mathrm{q}]/\hbar\right]}. \tag{5.19}$$

Here, the $\oint$ symbol simply denotes that the starting and end points are the same, and therefore the action must be taken over periodic paths. In order to determine Z we also must define a Hamiltonian H given by:

$$H = H_S + H_B + H_{SB} \tag{5.20}$$

where

$$H_S = \frac{p^2}{2M} + V(q) \tag{5.21}$$

is the system Hamiltonian for mass M and potential $V(q)$,

$$H_B = \sum_i \left[\frac{p_i^2}{2m_i} + \frac{m_i}{2}\omega_i^2 x_i^2 \right] \tag{5.22}$$

is the bath Hamiltonian, for N harmonic oscillators, and

$$H_{SB} = -q\sum_i^N c_i x_i + q^2 \sum_i^N \frac{c_i^2}{2m_i\omega_i^2} \tag{5.23}$$

is the Hamiltonian describing the coupling between the two. Applying the Heisenberg equation of motion (5.24) to 5.20,

$$\frac{\mathrm{d}A}{\mathrm{d}t} = \frac{\mathrm{i}}{\hbar}\left[H, A\right] \tag{5.24}$$

we find that this degree of freedom obeys the relation

$$\ddot{q} + \frac{1}{M}\left(\frac{\mathrm{d}V}{\mathrm{d}t} + q\sum_{i=1}^N \frac{c_i^2}{m_i\omega_i^2}\right) = \frac{1}{M}\sum_{i=1}^N c_i x_i \tag{5.25}$$

and for the bath:

$$\ddot{x} + \omega_i^2 x_i = \frac{c_i}{m_i} q(t). \tag{5.26}$$

Now solving equation 5.26 using a Greens function method to evaluate the response to its coupling with the system (we assume the bath modes are independent of each other) as well as its initial conditions, we see that

$$x_i(t) = x_i(0)\cos(\omega_i t) + \frac{p_i}{m_i\omega_i}\sin(\omega_i t) + \int_0^t ds \frac{c_i}{m_i\omega_i}\sin\left(\omega_i(t-s)\right) q(s). \tag{5.27}$$

Inserting this function into 5.25, we find that

$$M\ddot{q} + M\int_0^t ds\gamma(t-s)\dot{q}(s) + \frac{\mathrm{d}V}{\mathrm{d}q} = \xi(t) \tag{5.28}$$

where $\gamma(t)$ is the damping kernel given by

$$\gamma(t) = \frac{1}{M}\sum_{i=1}^{N}\frac{c_i^2}{m_i\omega_i^2}cos(\omega_i t) \tag{5.29}$$

and $\xi(t)$ is the inhomogeneity, or bath driving which takes the form

$$\xi(t) = \sum_{i=1}^{N}\left[\left(x_i(0) - \frac{c_i}{m_i\omega_i^2}q(0)\right)\cos(\omega_i t) + \frac{p_i(0)}{m_i\omega_i}\sin(\omega_i t)\right]. \tag{5.30}$$

So far, we have explored the relationship between the system and an arbitrary, but finite number of bath modes. Suppose we characterize the ensemble of bath modes given in 5.29 by a spectral density of bath modes. For a discrete number of such bath modes with characteristic frequencies, this spectral density takes the form of a sum over Dirac functions

$$J(\omega) = \pi\sum_{i=1}^{N}\frac{c_i^2}{2m_i\omega_i}\delta(\omega - \omega_i) \tag{5.31}$$

and the damping kernel can be expressed as

$$\gamma(t) = \frac{2}{M}\int_0^\infty \frac{d\omega}{\pi}\frac{J(\omega)}{\omega}\cos(\omega t). \tag{5.32}$$

With appropriate choices of c_i, m_i, ω_i (which can be chosen phenomenologically) the spectral density can take various forms depending on the type of dissipation we intend to model; for example, if we set $J(\omega) = M\gamma\omega$, we find that $\gamma(t) = 2\gamma\delta(t)$

and equation 5.28 reduces to the usual memory-less equation of motion with forcing $\xi(t)$, potential $V(q)$, and damping occurring only 'locally' -i.e. instantaneously- in time with strength $\gamma(t) = \gamma\delta(t)$, (the integration over s, terminating at time t, stops *half-way* through the delta function, contributing one-half.) Although the ohmic spectral density discussed above may work well in principle, it diverges for large ω, hence, practical models require some high-frequency cut-off. To this end, the Drude model is proposed:

$$J(\omega) = M\gamma\omega\frac{\omega_D^2}{\omega^2 + \omega_D^2} \tag{5.33}$$

which is linear for small ω, but tends smoothly to zero as ω exceeds ω_D. For finite ω_D we find that damping is not exclusively instantaneous, or 'local', but that

$$\gamma(t) = \gamma\omega_D \mathrm{e}^{[-\omega_D t]}, \tag{5.34}$$

hence, our model gives rise to memory effects on the order of $t < \omega_D^{-1}$. If we take ω_D to be sufficiently large, and are not interested in time scales shorter than it's reciprocal, then these memory effects can be neglected and the Drude model reduces to the Ohmic model.

5.3 Tracing out the bath coordinates

The Euclidean action determined in 5.17 contains extra terms when the system is coupled to a bath of harmonic oscillators (S^E in equation 5.18.) each of which can be separated into components describing the system (S), bath(B), and coupling between each (SB) as follows:

$$S^E[q, x_i] = S_S^E[q] + S_B^E[x_i] + S_{SB}^E[q, x_i] \tag{5.35}$$

with

$$S_S^E[q] = \int_0^{\hbar\beta} d\tau \left(\frac{M}{2}(\dot{q})^2 + V(q)\right) \tag{5.36}$$

$$S_B^E[x_i] = \int_0^{\hbar\beta} d\tau \sum_i \frac{m_i}{2}\left(\dot{x}_i^2 + \omega_i^2 x_i^2\right) \tag{5.37}$$

and

$$S^E_{SB}[q, x_i] = \int_0^{\hbar\beta} d\tau \left[-q \sum_i c_i x_i + q^2 \sum_i^N \frac{c_i^2}{2 m_i \omega_i^2} \right]. \tag{5.38}$$

Note that both equation (5.37) and (5.38) can be conveniently expressed into one action which we call the 'influence' action of a single bath oscillator

$$S^E_{infl}[q, x_i] = \int_0^{\hbar\beta} d\tau \frac{m_i}{2} \left[\dot{x}_i^2 + \omega_i^2 \left(x_i - \frac{c_i}{m_i \omega_i^2} q \right)^2 \right]. \tag{5.39}$$

Moreover, the actions associated with each of the system and bath coordinates can be factorized from the exponential argument as follows:

$$\oint Dq \mathrm{e}^{[\mathrm{S_S[q]+S_1[q,x_1]+S_2[q,x_2]+...}]} = \oint \mathrm{Dq e^{[S_S[q]]} e^{[S_1[q,x_1]]} e^{[S_2[q,x_2]]}} \times \ldots \tag{5.40}$$

Hence, we define a functional for each bath oscillator $F_i[q]$

$$F_i[q] = \int dx_i \oint Dx_i \mathrm{e}^{\left[-\frac{1}{\hbar} \mathrm{S^E_{infl}[q,x_i]}\right]} \tag{5.41}$$

and an overall influence functional

$$F[q] = \prod_{i=1}^{N} \frac{1}{Z_i} F_i[q]. \tag{5.42}$$

Equation 5.42 contains all the information of the influence of the bath as a whole on the system. As shown in appendix C, we can determine the influence functional to be

$$F[q] = \exp^{\left[-\frac{1}{2\hbar} \int_0^{\hbar\beta} d\tau \int_0^{\hbar\beta} d\sigma k(\tau-\sigma) q(\tau) q(\sigma) \right]} \tag{5.43}$$

and thereby determine our final partition function. We will restrict ourselves to considering the region above the crossover temperature, where only the stationary solutions $q = 0$, and $q = q_B$ contribute to our partition function, and the bounce, or instanton solution can be ignored. The end result is then

$$
\begin{aligned}
Z &= \oint Dq\mathrm{e}^{\left[-\mathrm{S^E[q]}/\hbar\right]} = \oint_{\mathrm{q=0}} \mathrm{Dqe}^{\left[-\mathrm{S^E[q]}/\hbar\right]} + \oint_{\mathrm{q=q_b}} \mathrm{Dqe}^{\left[-\mathrm{S^E[q]}/\hbar\right]} \\
&= \frac{1}{\omega_0}\sqrt{\frac{2\pi}{M\beta}}\prod_{n=1}^{\infty}\frac{\pi}{\frac{M\beta}{2}\left(\nu_n^2+|\nu_n|\hat{\gamma}(|\nu_n|)+\omega_0^2\right)} \\
&- \frac{\mathrm{i}}{2\omega_b}e^{-\beta V_b}\sqrt{\frac{2\pi}{M\beta}}\prod_{n=1}^{\infty}\frac{\pi}{\frac{M\beta}{2}\left(\nu_n^2+|\nu_n|\hat{\gamma}(|\nu_n|)-\omega_b^2\right)}
\end{aligned}
\tag{5.44}
$$

where ν_n are the Matsubara frequencies (see appendix C.)

Here, the real and imaginary components of the partition function are clearly separated. If we further assume that $\beta V_b \gg 1$ then we may apply the same reasoning as in equations 5.6 through 5.8 to deduce the imaginary part of the free energy, and thereby the escape rate k.

$$
k = \frac{-2}{\hbar}\mathrm{ImF} = \frac{-2}{\hbar\beta}\frac{\mathrm{Z_b}}{\mathrm{Z_0}} = \frac{\omega_0}{\hbar\beta\omega_\mathrm{b}}\mathrm{e}^{[-\beta\mathrm{V_b}]}\prod_{\mathrm{n=1}}^{\infty}\frac{\nu_\mathrm{n}^2+\nu_\mathrm{n}\hat{\gamma}(\nu_\mathrm{n})+\omega_0^2}{\nu_\mathrm{n}^2+\nu_\mathrm{n}\hat{\gamma}(\nu_\mathrm{n})-\omega_\mathrm{b}^2}. \tag{5.45}
$$

Figure 5.3 shows an Arrhenius plot of the escape rate vs. temperature determined from the methods discussed in this chapter, and the previous, for the metastable well with $V_B = 0.016E_J$, a two-level system. Ingold cites a crossover temperature, $T_0 = \frac{\hbar\omega_b}{2\pi k_B}$, separating the regions where the barrier crossing process is dominated by thermal excitation, and quantum tunnelling respectively; a crossover which we see clearly between the results of equation 5.10 and 4.25. At large temperature, figure 5.3 shows large discrepancies between the tunnelling average, and the classical rate, as expected, since the former does not account for states that would otherwise have significant populations –the latter is the more trust-worthy result. The classical Kramer's result, however, is still in disagreement with the results of equation 5.45 by a factor of approximately 4-5. The reason for this is most likely the fact that equation 5.45 accounts only for the extremal positions that yield stationary points in the Euclidean action, and therefore do not account for the nonlinear aspects of our potential. Also, for our potential V_B and $\hbar\omega_0$ differ by about a factor of 3, undermining confidence in the Taylor expansion that we employed in equation 5.4, since we assumed $V_B \gg \hbar\omega_0$; since this assumption was also made in our classical escape rate, however, it must be noted that *all* escape rate calculations fail at sufficiently high temperature. [1]

Nevertheless, the IM-F method gives us the thermal-averaged tunnelling escape rate below T_0, to complement the classical escape rate we employ at higher temperature. The fact that the results of the IM-F method using the Matsubara expansion are not wildly disparate –despite the many approximations made above– adds credence to our calculations.

[1] Though at such temperatures, the device would have unacceptably high dark count rates, and we would have little interest in further investigation.

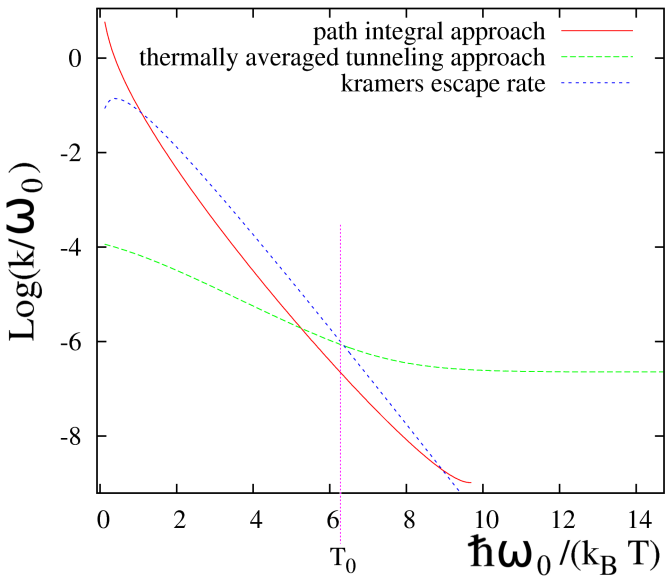

Figure 5.3: Arrhenius plot of the ratio between escape rate and harmonic frequency using the path integral approach (equation 5.45), the thermally averaged tunnelling rate (equation 5.10), and the classical Kramer's escape rate (equation 4.25) assuming Q=1 and a metastability with $V_B = 0.016E_J$. Note that the latter two intersect at almost precisely the crossover temperature $T_0 = \frac{\hbar\omega_b}{2\pi k_B}$; the thermally averaged tunnelling rate gives an excellent approximation to the zero-temperature tunnelling escape rate but breaks down when there is appreciable thermal excitation into states not accounted for with the expansion in equation 5.10. Equation 4.25, on the other hand, accounts for thermal excitation at finite temperature, until the assumption that $V_B \gg k_B T$ fails, at which point it too breaks down.

Chapter 6

Numerical simulation of the detection process

We have now seen several analytic models of the metastable escape process, due to thermal excitation, quantum tunnelling, and direct current drive. Each of these models contains some of the aspects of our detection process, but a thorough representation of the entire system dynamics requires a numerical approach of the sort introduced by Larkin and Ovchinikov [25], and later developed by Chow, Browne and Ambegaokar [36, 37] –the latter of whom will be the focus of our attention.

6.1 Equations of motion.

Chow, Browne and Ambegaokar[36] consider a metastable Josephson circuit with sufficiently deep metastability to permit on the order of 'tens of levels' and restrict their consideration of the system to this region of flux as they develop a dynamic model for state transition and metastable escape. Hence, their model is equally applicable to systems which exhibit a tilted washboard potential (as considered by Romero et al [15]) as well as asymmetric bistability.

According to Larkin and Ovchinikov[25], low energy states deep in the well have finite escape amplitudes that are well approximated by the semiclassical formula

$$\Gamma_n \approx \frac{\mathrm{e}^{\left[\frac{2\mathrm{S_E(E_n)}}{\hbar}\right]}}{T(E_n)}, \tag{6.1}$$

where $T(E_n) = 2\oint \mathrm{dx}/\dot{\mathrm{x}}$ is the period of classical motion at energy E_n above the 'ground' state[1] and $S_E(E_n) = \oint p_E \mathrm{dq}$ is the Euclidean action under the barrier for

[1]the term 'ground state' is used loosely here, and refers to the lowest energy state confined to the metastable well, since the cited authors restrict their consideration of flux space to the metastable well, hence other states are unbounded.

states of that energy. However, the escape amplitude of these levels is exponentially suppressed in favour of levels with energy close to the barrier maximum. To calculate the escape rates of *these* states, a numerical approach that captures tunnelling and thermal effects must be employed.

Instead of restricting our region of interest to the metastable well and deriving escape rates as in Chow and Ambegaokar (CA) [37], our approach is to employ the same methodology while considering explicitly the states on the other side of the barrier; thus making our system bounded, unlike CA. To see this, we begin with equations 3.3 - 3.4 from reference [37], omitting the escape terms

$$\begin{aligned}
\dot{\hat{\rho}}_{jj} &= \frac{1}{\mathrm{i}\hbar}\langle j|\left[H_I,\hat{\rho}\right]|j\rangle + \sum_k W_{k\to j}\hat{\rho}_{kk} - \sum_k W_{j\to k}\hat{\rho}_{jj} \\
\dot{\hat{\rho}}_{jk} &= \frac{1}{\mathrm{i}\hbar}\langle j|\left[H_I,\hat{\rho}\right]|k\rangle - \frac{\hat{\rho_{jk}}}{2}\left(\sum_n \left(W_{j\to n}+W_{k\to n}\right)\right) + \sum_{l\neq j, m\neq k}\hat{\rho}_{lm}R_{jk;lm}.
\end{aligned} \tag{6.2}$$

Note that equation 6.2 is written in the interaction representation –that is to say, $H_I = \mathrm{e}^{\left[\frac{-\mathrm{iH_0t}}{\hbar}\right]}\hat{\phi}\mathrm{I(t)}\mathrm{e}^{\left[\frac{\mathrm{iH_0t}}{\hbar}\right]}$, with H_0 given in 3.3. The thermal transition rates $W_{j\to k}$ are given by

$$W_{k\to j} = \frac{2}{\hbar}|\phi_{jk}|^2 J(|\omega_{jk}|)\left[(1+n(\omega_j k))\,\Theta(\omega_{jk}) + n(\omega_{kj})\Theta(\omega_{kj})\right]. \tag{6.3}$$

Here $\hbar\omega_{jk} = E_j - E_k$, $n(\omega_{jk})$ is the Bose distribution, $J(\omega) = \frac{C_J\omega\omega_D^2}{Q\left(\omega^2+\omega_D^2\right)}$ is the spectral distribution of the oscillator bath, and Θ is the Heaviside function. The last summation in 6.2 represents the summation over the bath-induced off-diagonal coupling terms

$$R_{jk;pq} = \frac{\phi_{jp}\phi_{qk}}{\hbar}J(|\omega_{jp}|)\left[(1+n(\omega_{jp})) + n(\omega_{qk})(1+\omega_{qk})\right]. \tag{6.4}$$

Previous work [36] has shown that the contribution to 6.2 from equation 6.4 is generally negligible and we independently concur. As noted in chapter 3, the coupling strengths ϕ_{jk} of these states decrease exponentially with $|E_j - E_k|$, thus permitting us the numerical expedience of restricting our Hilbert space to states with energy near the barrier.

6.2 Measuring detection.

We use numerical solution methods on equation 6.2 analogous to those explored in chapter 2 and note that the probability distribution function in ϕ and time can then be written as

$$\alpha(\phi, t) = \sum_n \rho_{nn}(t) \left|\langle\phi|\Psi_n\rangle\right|^2 \tag{6.5}$$

using the basis of energy eigenstates $\hat{H}_0|\Psi_n\rangle = E_n|\Psi_n\rangle$, determined in chapter 3. Furthermore, we define the switching probability P_s as the likelihood that the system has transitioned to the other side of the barrier:

$$P_s(t) = \int_{\phi'}^{\infty} \alpha(\phi, t)\mathrm{d}\phi \tag{6.6}$$

where ϕ' is the position of barrier maximum. Hence, while the CA method defines escape as the loss of probability from the region of interest, we maintain probability conservation and explicitly calculate the full probability distribution as a function of flux. The barrier maximum ϕ' is then a natural coordinate to choose as a threshold delineating the bound of our detection criteria since states that are excited to this level will decay (and therefore be diverted away from this position) along a time scale given, at most, by

$$\tau = 2\pi Q \left(\frac{1}{\omega_a} + \frac{1}{\omega_c}\right). \tag{6.7}$$

In (6.7) we have taken $\frac{2\pi}{\omega_a} + \frac{2\pi}{\omega_c}$ as an upper-bound to the period of oscillation throughout the anharmonic double well, assuming no critical slow-down in the region of the barrier maximum. We now define the electric current applied to the circuit via the Hamiltonian $H_I(t)$ in equation 6.2 as a sinusoid with a Gaussian envelope:

$$I(t) = A\mathrm{e}^{\left[-\frac{(\mathrm{t}-\mu)^2}{2\sigma^2}\right]} \sin(\omega_{\mathrm{R}}\mathrm{t}) \tag{6.8}$$

where σ is as yet unconstrained. Since σ describes the temporal width of the pulse, the amplitude A is constrained by energy conservation, which we maintain by performing integration over equation 3.5 [29]

$$\int_{-\infty}^{\infty} \frac{A^2}{2}\mathrm{e}^{\left[-\frac{(\mathrm{t}-\mu)^2}{\sigma^2}\right]} \sin^2(\omega_{\mathrm{R}}\mathrm{t}) = \hbar\omega_{\mathrm{R}}. \tag{6.9}$$

We may now show the reasons behind the ostensibly arbitrary choice of circuit components C_J, L_s, and biasing ϕ_x introduced in chapter 3 which led to the barrier height of $V_B = 0.016E_J$ that we have been assuming throughout much of the preceding discourse. In so doing, we will also determine the optimal quality factors, and temporal pulse widths for our detector. By 'optimal' parameters, we mean that

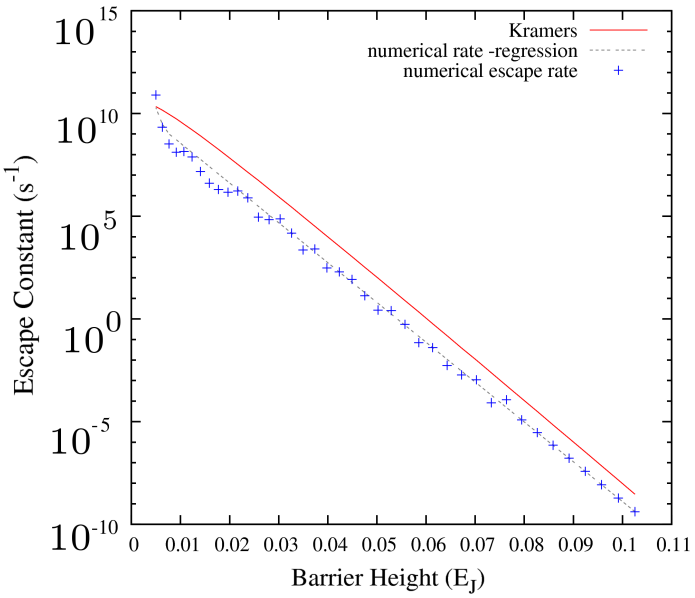

Figure 6.1: The exponential constant k_D of equation 6.10 as a function of barrier height, assuming a quality factor of unity (k_D scales inversely with Q.) In the limit of $V_B \to 0$ this quantity diverges, but we may draw a piece-wise best fit to it over the region of our interest.

which will maximize the probability of legitimate detection due to a single photon, while minimizing the likelihood of false-positive detection due to ambient noise. We assume the the process of photodetection is effectively complete after a time-scale of $t_1 = 4\sigma + 4\tau$ [2] and seek to minimize the probability of false-positive detection over this time scale. Hence, we designate the following joint probability P_J as the measure of success for various parameter designs

$$P_J = \left(\int_{\phi_b}^{\infty} \alpha(\phi, t_1) \mathrm{d}\phi \right) \times \left(1 - \mathrm{e}^{[-\mathrm{k_D}(\mathrm{V_B})\mathrm{t_1}]} \right). \tag{6.10}$$

The exponential escape constant k_D has been determined already by a number of different methods; we may determine this constant again empirically, by evolving a metastable system along equation 6.2, with current set to zero, and measure the decay rate of $\int_{-\infty}^{\phi'} \alpha(\phi, t) d\phi$ –the likelihood that the system remains metastable. We then compare this decay constant with the reaction coefficient determined using equation 4.25. The resulting plot is shown in figure 6.1

Given our dark escape constant as a function of barrier height, we are now in a position to predict the false-positive probability for a given time interval at a

[2] a time scale chosen somewhat arbitrarily, but based on the observation that the lingering solution leaves only a $\mathrm{e}^{[-4]} \approx 2$ % error residual

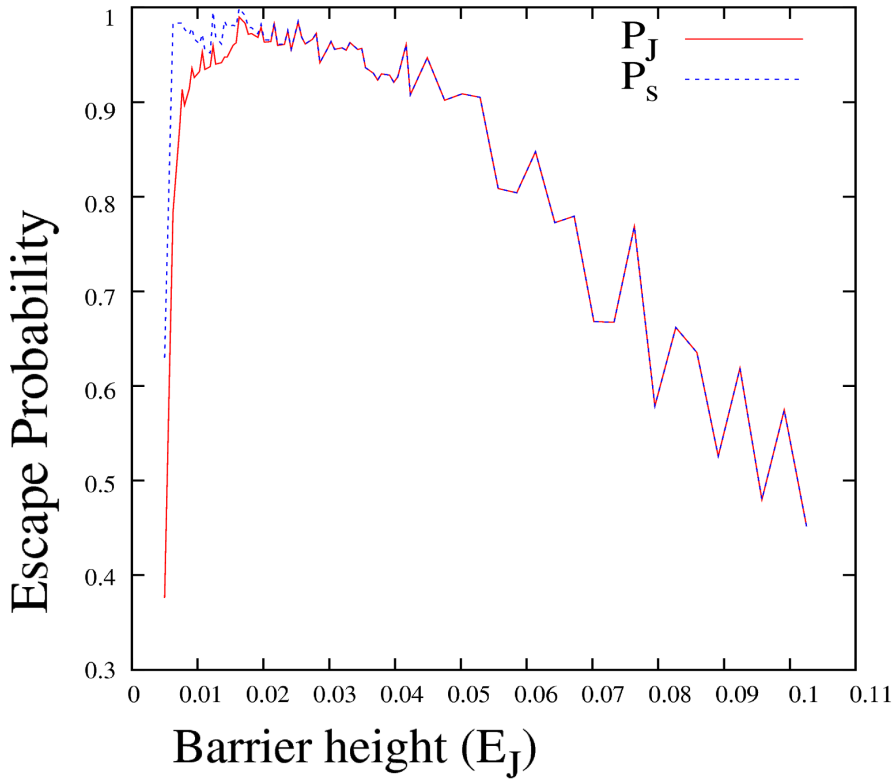

Figure 6.2: P_J and P_s as functions of the barrier height, in units of E_J; above $V_B \approx 1.5E_J$ dark counts are essentially negligible, and the two probabilities are identical. Note that the 'spikes' in this quantity (having the appearance of noise) are actually due to resonant tunnelling processes, and coincide precisely with potential arrangements in which the highest-energy metastable state is closely matched to an energy state on the opposite side of the barrier. The precipitous drop in P_s is due to the loss of coupling to other metastable states, and has been observed experimentally according to personal correspondence with J. Martinis.

specific barrier height – i.e. the second factor in equation 6.10. We then determine the first factor by returning to equations 6.2, and 6.5. Figure 6.2 shows a plot of the maximal quantity 6.10, and of the raw transition probability as a function of barrier height V_B after scanning over the pulse width and quality factor for optimal σ and Q – that is to say, each datum in figure 6.2 corresponds to a different value of Q and σ –each determined to be ideal for that V_B after a scan throughout the 2-dimensional $\sigma - Q$ surface. Comprehensive sampling of this parameter space was by far the most challenging and time-consuming component of this work; see appendix D for a synopsis of what was necessary to overcome this challenge. Naturally, with increasing barrier height, larger numbers of localized states are able to be confined in the well; figure 6.3 shows a plot of the number of confined metastable states against the height of the barrier, V_B.

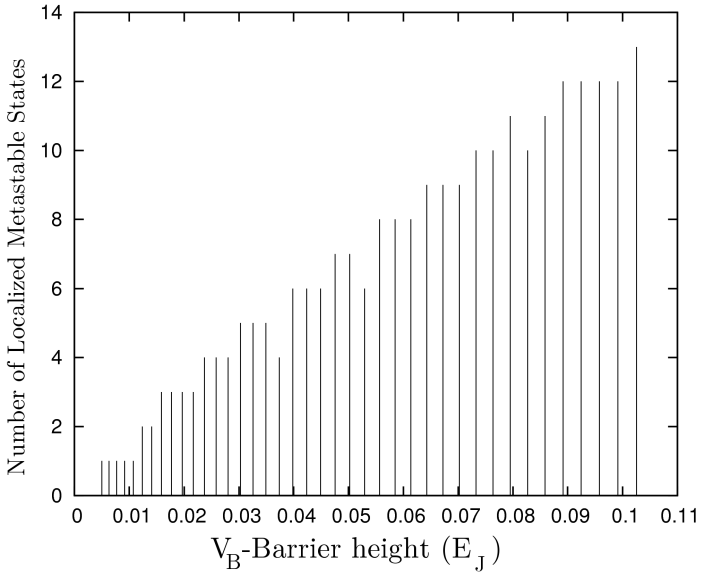

Figure 6.3: The number of confined metastable states as a function of the barrier height, V_B. We define a state $|\Psi_n\rangle$ to be metastable iff for potential $V(q)$ the state has energy $V(q_A) < E_n < V(q_B)$, and a wave function profile such that $\langle\Psi_n|\hat{q}|\Psi_n\rangle < q_B$ (see figure 5.1.) Naturally, the number of states increases with V_B, and our optimum parameter set occurs when we have a two-level system. It should be noted, however, that the barrier height is mainly controlled by the external flux, a parameter that also has a minor effect on the *width* of the metastable well. The fact that increasing the bias not only increases the barrier height, but also contracts the spatial width of potential well, could account for the fact that the number of confined states is not perfectly monotonically increasing in the figure.

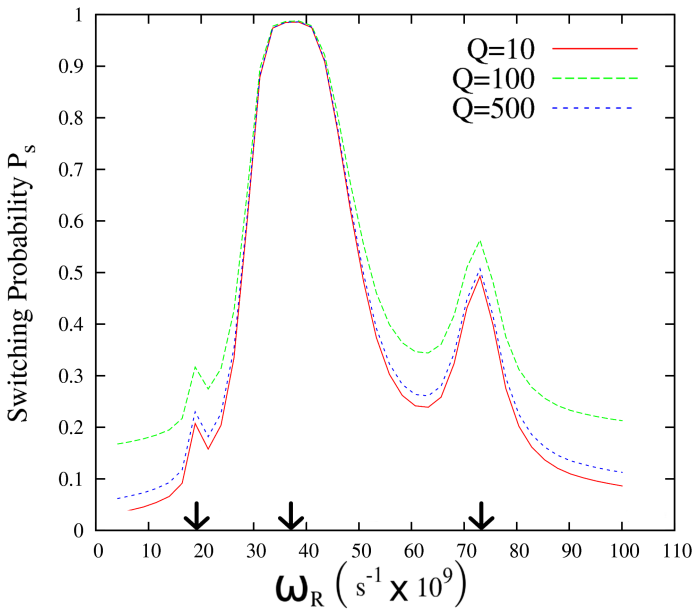

Figure 6.4: Transition probabilities as a function of drive (photon) frequency for various quality factors; note the response peaks at $\omega = 37, 19.1$, and 73.2 Grad/s –in excellent agreement with the resonance points determined in our classical model in chapter 4 (see figure 4.1 –these resonance points are indicated by arrows in the above figure.)

From the data in figure 6.2 it is clear that the optimal barrier height for this trade-off is at $V_B = 0.016E_J$. Although the erratic jumps in the lines in figure 6.2 have the appearance of noise, this is actually the result of resonant tunnelling –an effect that occurs when the more energetic states in the metastable well are closely matched in energy to states on the other side of the barrier. To reduce the dimensionality of parameter space which we were required to scan over, the above optimizations were performed assuming an ideal drive frequency given by a harmonic approximation.

Having optimized the detector over the pulse-width, barrier height, and dissipation rate we must then determine the sensitivity of the detection mechanism to changes in the drive frequency, or the bandwidth of the detector. Figure 6.4 shows that although the optimum drive frequency is slightly red-shifted from the harmonic approximation, the bandwidth is amply wide enough to include the harmonic frequency, validating the optimization procedure used above. We also observe a bandwidth of 25.4 Grad/s, or 4 GHz. In fact, not only is our proposed detector effective over a wide range of frequencies, but also over σ, and Q as well, as seen in figure 6.5.

One possible explanation for the robustness of our model over the above parameters is that our detection scheme relies on irreversible decoherence, and is not dependent on any particular intermediary states –the parameters of the photon

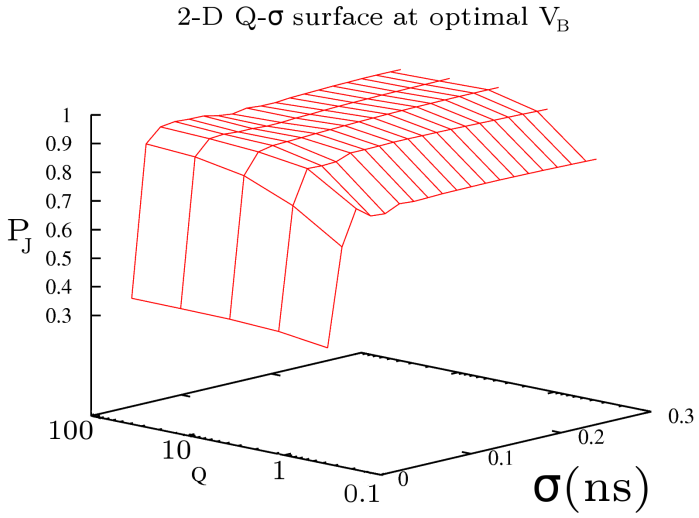

Figure 6.5: Joint probability P_J (see 6.10) across the barrier, after photon absorption, as a function of the quality factor of the resonator (Q,) and the pulse-width of the photon (σ) for the optimal barrier height $V_B = 0.016E_J$. Note the robustness of this value in the ranges $\sigma > 0.05$ns, and $Q > 5$; clearly demonstrating a great deal of flexibility in the values of these parameters.

and circuit do not then need to be tuned to accommodate such specific states. For example, over the range of frequencies in the bandwidth shown in figure 6.4, the transition across the barrier is mediated by a variety of different intermediary states, the population of each depending on its energy difference from the initial state, and how well this difference is matched to the frequency of the photon. Similarly, with large Q-values, incoming energy from the photon is better conserved, while lower Q values entail level-broadening which facilitates tunnelling and other transitions. Since we are neither concerned with how the barrier-crossing is mediated, nor about which states act as intermediaries, we can assume a great deal of latitude in our choices of Q, and ω_R –the different mechanisms by which these different parameter sets give rise to transition is of no concern to us, so long as the bulk of systems probability distribution crosses the barrier by one of the above methods.

The dependence of P_J on σ is a bit more nuanced; we find that P_s decays exponentially with σ for large V_B, hence short, intense bursts of radiation are strongly preferred, though the rate at which P_s decays with σ varies depending on Q. As the barrier is reduced, P_s becomes effectively independent of σ, as we can see in figure 6.6. For the optimal barrier height determined above, the strong σ-dependence has disappeared implying a great deal of flexibility in σ as well.

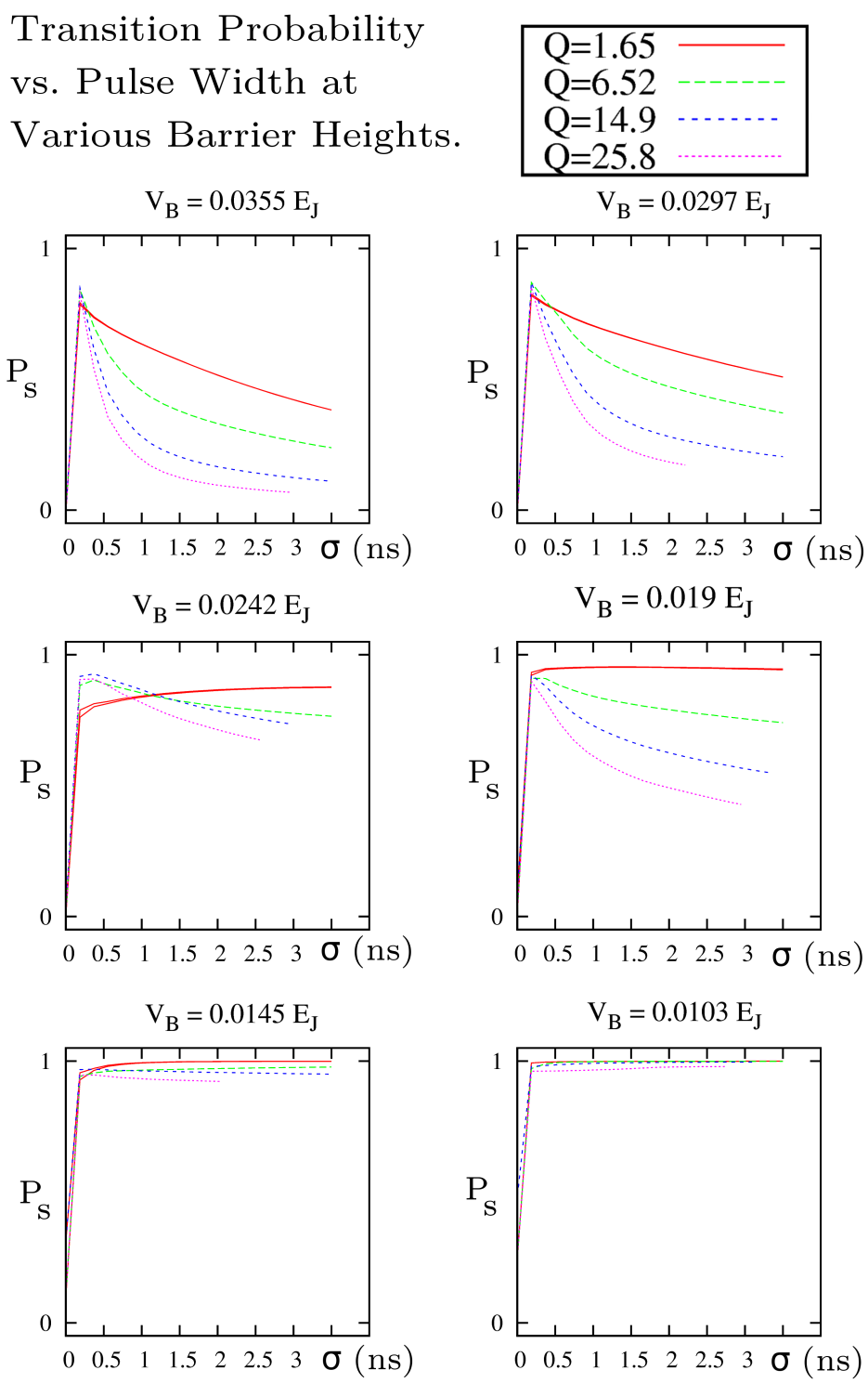

Figure 6.6: Raw transition probability (P_S, ignoring dark count rates), as a function of the pulse width σ, in nanoseconds, for various barrier heights V_B. Note that with large barriers, transition favours short, intense pulses, while with more shallow metastabilities, the transition probability is essentially independent of the pulse width.

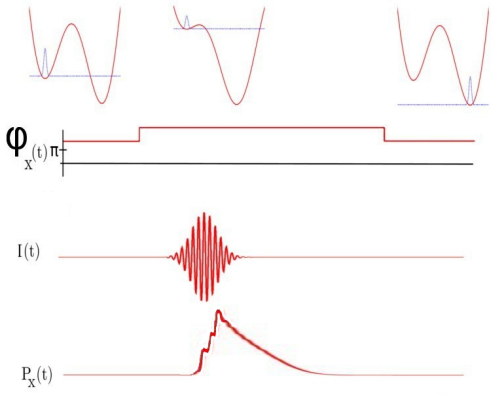

Figure 6.7: Time-line of the detection process; when a photon is anticipated, the biasing flux is momentarily increased to reduce the effective barrier height to the optimum value determined above and increase the system's sensitivity. W

6.3 Discussion

The results of the optimization process shown in figure 6.2 indicate that the optimum potential profile for detection does not permit standing detection. The size of the potential barrier is more similar to that of figure 4.8 than that of figure 4.9, and the dark counts predicted from figure 6.1 indicate that the mean life-time of this circuit is too short to be used as a standing photon-detector. Hence, a pulse protocol is necessary, this entails biasing the external flux for a window of time to detect photons as shown in figure 6.7.

It should be noted that this assertion can only be made under the assumption that the detector is subjected to an ambient temperature of 0.1K. Should a lower temperature be obtained, mean metastable lifetimes of detectors at the barrier heights described above would be greatly enhanced.

Nevertheless, we fully optimize the detector and show the robustness of our detection scheme to changes in the aforementioned parameters for our assumed operating temperature of 0.1K. It should also be noted that with increasing V_B, higher Q-values tend to be preferred since it is necessary to preserve the photon's energy to surmount the barrier. However, time-limitations prevented a thorough scan of Q-values above approximately 100, hence it is quite possible that data points to the right of $V_B = 0.016E_J$ in figure 6.2 could be pushed upward with additional scans. Nevertheless, with the scan of parameter space we have performed, we obtained a fidelity of $P_J = 98\%$, and it is possible that this number could be improved upon. To see the detection process in action with these idealized parameters, we plot band probabilities for the state in figure 6.8 as a function of time against the applied current for two different Q values. The pronounced probability of excitation into the band of levels with energy above the top of the barrier for the higher Q value makes it clear that this transition is mediated primarily by

excitation above the barrier, and not quantum-mechanical tunnelling through it; for lower Q, the transition process seems to take place through a combination of *both* excitation/decay, and quantum tunnelling –the discrepancy in the mechanism of transfer for these two scenarios is accounted for by level broadening of the low-Q system, thus facilitating tunnelling.

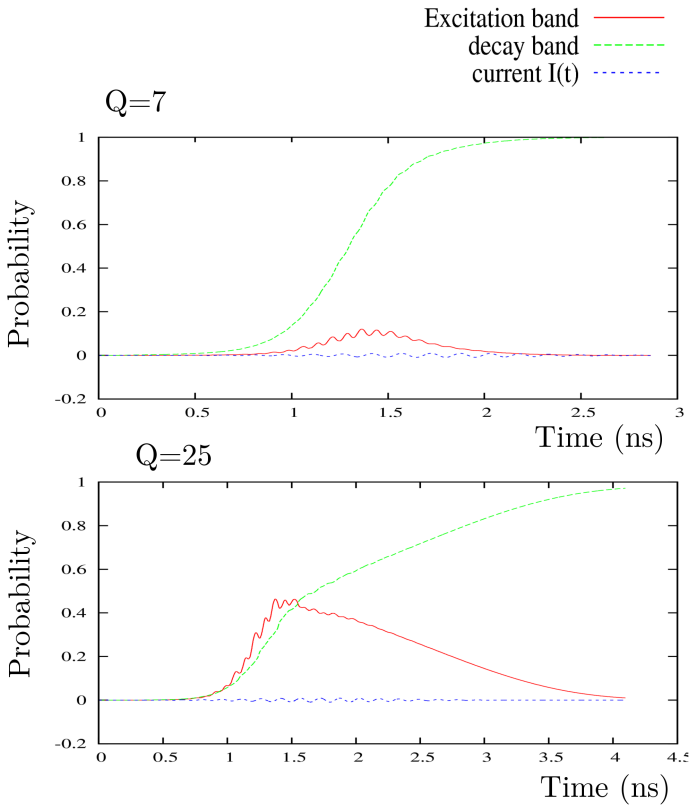

Figure 6.8: The cumulative probabilities of the system being in any of the states with energy above the barrier peak (the excitation band), any of the states with energy below the metastable basin (the decay band), and the current $I(t)$ driving these transitions. Note the differences in the population of the excitation band between the two Q-values; for $Q \leq 7$ significant barrier transition is achieved despite little population in the excitation band –this is due to a combination of two effects: (1) excitation band levels decaying very rapidly, and (2), level broadening with decreased Q permitting greater tunnelling. With $Q = 25$, slightly lower transition probability is achieved, despite significantly greater population of the excitation band. Evidently, optimal transition is achieved with a combination of both excitation/decay and tunnelling processes.

Chapter 7

Conclusion

In this work, we have seen that superconducting circuits, coupled to resonant cavities present great promise as a medium for quantum information. The existing work [7] that has been established on the coupling mechanisms between transmission lines and qubits has shown that single photons can be generated with the quantum state transitions of qubits -artificial atoms, for example- but that there remains to be seen a design of a device capable of detecting these photons, once generated.

Hence, we proposed a parallel circuit model with a nonlinear Josephson inductor to create a bistable potential in the branch-flux. To detect the arrival of a photon, we scan out the parameter space of the components of this circuit to ensure that reliable detection can be made while limiting the effects of extraneous false-positives, or 'dark counts.' We then developed increasingly sophisticated models to capture the dynamics of this process.

In chapter 2 we showed that a common model for optical photodetection [16] can be reproduced computationally, and we proved that such a numerical approach produced results that were consistent on short time-intervals with analytic results using perturbation theory.

We then showed, in chapter 3, how the discrete variable representation [17] can be used to determine position-space wave functions of eigenstates in an arbitrary potential, and why this solution method is preferable to a harmonic basis expansion. We also showed that the coupling strengths between the various eigenstates in such a system decreases exponentially with the energy difference between them, and that any excitation that may occur, would therefore be limited to a relatively small group of energy levels –thus permitting us to truncate the dimensionality of our Hilbert space in the dynamic equations employed in chapter 6.

In chapter 4 we ignored the discrete energy solution set, and considered a purely classical model. We showed that the perturbative expansion of anharmonic systems generally gives rise to multiple resonance frequencies characterized by simple geometric fractions of the harmonic approximation taken at local minimum of the

potential. This analytic result was borne out in classical computational time evolution simulations showing local minima, in frequency space, of the drive amplitude necessary to achieve transition over a barrier for a point particle. The frequencies at which we observed these resonant responses exhibit excellent agreement with the resonance peaks of the transition amplitude determined by our quantum mechanical model in chapter 6. We then derived the classical escape rate by considering a steady-state probability distribution in energy for a metastable system –this escape rate was then shown to be in excellent agreement with the escape rates observed from our quantum mechanical model in the absence of any drive mechanism due to a photon. Using this classical model we then showed the dependence of the mean life time of the metastable system on the quality factor of the resonator, and the ambient temperature.

In chapter 5 we showed how stationary points in the action of imaginary time path-integrals can be used to determine escape rates of metastable systems via the Im-F method –results which we showed are within a factor of 5 of escape rates determined using the methods described above. We also showed how the Im-F method can be used to justify taking a thermally-averaged tunnelling rate to determine the escape rate of the system below the crossover temperature, where transition is dominated by tunnelling, rather than thermal excitation. Since this method assumes instantaneous thermalization of the states energy distribution, however, and since it fails to account for non-linearities in the potential, its applicability to our model –outside of the low-Q limit–of photodetection is dubious, and we opt instead for escape rates determined from the other methods above.

In chapter 6 we presented the most noteworthy results of this study. We introduced our working model using density matrix of states in the DVR basis determined from chapter 3, and the equations of motion which we showed to be reliable in chapter 2. The quantum mechanical analog of these equations has two main components: the drive due to interaction with the photon, and the dissipation of energy from the circuit. We demonstrate the validity of the former by showing identical resonance peaks of the system with those determined from classical equations of motion, and of the latter by comparing the escape rate in absence of drive, and the Kramer's escape rate which we derived in chapter 4. We also proposed a quantity P_J, which we dubbed the fidelity, to measure our success in finding a compromise between the competing needs of detecting legitimate photons, and avoiding false-positives. Then, most importantly, after demonstrating the dependence of the barrier transition on σ, Q, V_B, and ω_R, we showed that with an optimal choice of these parameters, a transition probability of $P_s = 99.9\%$ can be achieved, as well as a fidelity of $P_J = 98.04\%$ assuming $Q = 7$, $\sigma = 0.6$ns, $V_B = 0.016E_J$, $\omega_R \approx 37G\text{rads}^{-1}$, though as figures 6.4, 6.5 and 6.6 indicate, we have a great deal of flexibility in these parameters.

It must be said that with further scanning of the above parameter space, this result may be improved further still –most likely by altering the parameters C_J and L_s, although these could only be altered with a concurrent lowering of the ambient temperature; temperatures of 20mK have been reported, and such temperature

ranges would greatly reduce dark counts, bringing our fidelity P_J closer in line with the raw switching probability P_s. This added dimensionality to our parameter space could improve our overall fidelity though it must be said that there is, in principle, no upper limit to the amount of time and computer resources that could be devoted to sampling this parameter space with ever-increasing scope and resolution.

Appendix A

The Fokker-Planck, and Kramer's Relations

We wish to derive the Fokker-Planck and Kramer's relations given in chapter 4, starting from the differential equations of motion for an arbitrary distribution $f(p,q)$

$$\begin{aligned}
&\frac{d}{dt}\iint_{-\infty}^{\infty} dp\,dq f(p,q)W(p,q,t) \\
&= \iint_{-\infty}^{\infty} dp\,dq\left[\frac{\partial f(p,q)}{\partial q}\left(\frac{dq}{dt}\right)\,dt\,+\frac{\partial f(p,q)}{\partial p}\left(\frac{dp}{dt}\right)\,dt\,+\mathcal{O}(dt^2)\right]W(p,q,t) \\
&= \iint_{-\infty}^{\infty} dp\,dq\left[p\frac{\partial f(p,q)}{\partial q}\,dt+(-K(q)-\gamma p)\,\frac{\partial f(p,q)}{\partial p}\,dt+\mathcal{O}(dt^2)\right]W(p,q,t) \quad \text{(A.1)}
\end{aligned}$$

where $W(p,q,t)$ is the probability density function of p and q. We note that the first term on the right hand side of equation A.1 can be written as

$$\begin{aligned}
&\iint_{-\infty}^{\infty} dp\,dq\;\; p\frac{\partial f(p,q)}{\partial q}W(p,q,t)\,dt \\
&= \int_{-\infty}^{\infty} dp\left([p\,f(p,q)W(p,q,t)]_{q=-\infty}^{q=\infty}-\int_{-\infty}^{\infty} dq\;p\,f(p,q)\frac{\partial W(p,q,t)}{\partial q}\right)\,dt. \quad \text{(A.2)}
\end{aligned}$$

Similarly, the second term

$$\iint_{-\infty}^{\infty} dp\,dq\,(-K(q)-\gamma p)\,\frac{\partial f(p,q)}{\partial p}W(p,q,t)\,dt \quad \text{(A.3)}$$

can be written as

$$\int_{-\infty}^{\infty} dq \left([f(p,q)(-K(q)-\gamma p)W(p,q,t)]_{p=-\infty}^{p=\infty} - \int_{-\infty}^{\infty} dp\, f(p,q) \frac{\partial \left(W(p,q,t)(-K(q)-\gamma p)\right)}{\partial p} \right) dt. \tag{A.4}$$

At this point we impose boundary conditions on the system on physical grounds: it must be the case that $\lim_{p\to\pm\infty} W(p,q,t) = \lim_{q\to\pm\infty} W(p,q,t) = 0$, both because of probability normalization constraints, and conservation of energy (since the above argument holds, even for an arbitrarily increasing potential -not just the one sketched in figure 3.5 - having finite distribution at these limits would violate energy conservation.) Therefore, the terms of integration limits in expressions A.2 and A.4 can be neglected.

Expression A.5 then reduces to

$$\int_{-\infty}^{\infty}\int dq\, dp \left(f(p,q)K(q)\frac{\partial W(p,q,t)}{\partial p} + \frac{\partial \left(W(p,q,t)\gamma p\right)}{\partial p} \right) dt. \tag{A.5}$$

Equating 4.13 to A.2 and A.5 we obtain

$$\begin{aligned} \frac{d}{dt}\int_{-\infty}^{\infty}\int dp\, dq\, f(p,q)W(p,q,t) &= \int_{-\infty}^{\infty}\int dp\, dq \left(-p\, f(p,q)\frac{\partial W(p,q,t)}{\partial q} + \right. \\ &+ \left. f(p,q)K(q)\frac{\partial W(p,q,t)}{\partial p} + \gamma\, f(p,q)\frac{\partial \left(p\, W(p,q,t)\right)}{\partial p} \right). \end{aligned} \tag{A.6}$$

Now recall that $f(p,q)$ is an *arbitrary* function. We could very easily choose a $f(p,q)$ that is zero everywhere with the exception of an infinitesimal region $dp\, dq$, and equation A.6 must still hold; hence we set the integrands themselves in equation A.6 equal. if we then choose $f(p,q) = 1$ we see that:

$$\frac{\partial}{\partial t}W(p,q,t) = -p\,\frac{\partial W(p,q,t)}{\partial q} + K(q)\frac{\partial W(p,q,t)}{\partial p} + \gamma\,\frac{\partial \left(p\, W(p,q,t)\right)}{\partial p}. \tag{A.7}$$

Equation A.7 gives us the Fokker-Planck equation, assuming no external noise is applied to the system. We must now return to relations 4.8 - 4.10 and consider the same case with finite N, thereby introducing stochastic driving $\xi(t)$.

A.1 with thermal drive

The same expansion we employed in expression 4.14, now requires us to include 2nd-order derivatives of 'f' to expand to 1rst order in dt, since under the Ito interpretation $dw^2 = dt$

$$\begin{aligned}
&\iint_{-\infty}^{\infty} \frac{dp\,dq}{dt}\left[\frac{\partial f(p,q)}{\partial q}\left(\frac{dq}{dt}\right)dt + \frac{\partial f(p,q)}{\partial p}\left(\frac{dp}{dt}\right)dt + \frac{\partial^2 f(p,q)}{2\partial p^2}\left(\frac{dp}{dt}\right)^2 (dt)^2 + \ldots\right] W(p,q,t) \\
&= \iint_{-\infty}^{\infty} \frac{dp\,dq}{dt}\left[p\frac{\partial f(p,q)}{\partial q}\,dt + (-K(q) - \gamma p)\,\frac{\partial f(p,q)}{\partial p}\,dt\right. \\
&\left. + \sqrt{N}\frac{\partial f(p,q)}{\partial p}dw + \frac{N}{2!}\frac{\partial^2 f(p,q)}{\partial p^2}\,dw^2 + \mathcal{O}(t^2)\right] W(p,q,t) \qquad \text{(A.8)}
\end{aligned}$$

Note that the first order derivative $\frac{\partial f}{\partial p}\frac{dp}{dt}$ contain a term of order dw, but since w has zero mean, this term vanishes when averaged over; $dw^2 = dt$, however, has finite mean. The last term in expression A.8 can be treated similar to the above:

$$\begin{aligned}
\int\!\!\!\int_{-\infty}^{\infty} dp\,dq\frac{\partial^2 f}{\partial p^2}\left(\frac{N}{2} + \mathcal{O}(dt^2)\right) W(p,q,t) &= \frac{N}{2}\int_{-\infty}^{\infty} dq\left[\left[W\frac{\partial f}{\partial p}\right]_{p=-\infty}^{p=\infty} - \left[f\frac{\partial W}{\partial p}\right]_{p=-\infty}^{p=\infty}\right. \\
&\left. + \int_{-\infty}^{\infty} dp\, f\frac{\partial^2 W}{\partial p^2}\right]. \qquad \text{(A.9)}
\end{aligned}$$

Again, the limits terms can be neglected. Incorporating this term into our previous analysis of A.6, we arrive at

$$\frac{\partial}{\partial t}W(p,q,t) = K(q)\frac{\partial W(p,q,t)}{\partial p} - p\,\frac{\partial W(p,q,t)}{\partial q} + \frac{\partial}{\partial p}\left(\gamma\, p\, W(p,q,t) + \frac{N}{2}\frac{\partial W(p,q,t)}{\partial p}\right). \qquad \text{(A.10)}$$

This is the Kramer's relation cited in equation 4.18.

Appendix B

The Classical Escape Rate.

Having defined the magnitude of thermal perturbation N as $2\gamma k_B T$, we return to the partial differential equations given in chapter 4 in the action dimension

$$\frac{\partial \rho}{\partial I} + \frac{\omega(I)\rho}{2\pi k_B T} = \frac{-J\omega(I)}{2\pi\gamma I k_B T}. \tag{B.1}$$

Recall that all first order differential equations of the form

$$\frac{\partial y}{\partial x} + f(x)y = g(x) \tag{B.2}$$

can be expressed in the form

$$\frac{\partial}{\partial x}\left(yP(x)\right) = g(x)P(x) \tag{B.3}$$

where $P(x) = e^{\int f(x)\,dx}$. Hence, we simplify B.1 to:

$$\frac{\partial}{\partial I}\left(\rho \exp^{\left[\int_0^I \frac{\omega(I')}{2\pi k_B T} dI'\right]}\right) = \frac{-\omega(I)J}{\gamma I 2\pi k_B T} \exp^{\left[\int_0^I \frac{\omega(I')}{N} dI'\right]} \tag{B.4}$$

$$\therefore \rho(I) = -\exp^{\left[-\int_0^I \frac{\omega(I')}{2\pi k_B T} dI'\right]} \frac{J}{\gamma 2\pi k_B T} \int_0^I \frac{\omega(I''')dI'''}{I'''} \exp^{\left[\int_0^{I'''} \frac{\omega(I'')}{N} dI''\right]} + C. \tag{B.5}$$

We now apply equation 4.23 to the exponential arguments in B.5 to obtain:

$$\therefore \rho(I) = -\exp^{\left[-\frac{1}{k_B T}(E(I)-E(0))\right]} \frac{J}{\gamma 2\pi k_B T} \int_0^I \frac{\omega(I')dI'}{I'} \exp^{\left[\frac{1}{k_B T}(E(I')-E(0))\right]} + C. \tag{B.6}$$

Further, we impose boundary conditions on the system such that $\rho(I_B) = 0$, since we assume that as soon as particles obtain this energy they escape the system. Note that for any $f(x) = \int_0^x g(x')\,dx' + C$, if we wish to impose the condition that $f(x_0) = 0$, then we simply choose the integration constant C such that $C = -\int_0^{x_0} g(x')\,dx'$ leaving $f(x) = -\int_x^{x_0} g(x')\,dx'$. So it is with the integration constant C in B.6.

Also, since the reaction rate k is defined as the ratio of the probability current to the total population,

$$k = \frac{J}{n_0} = \frac{J}{\int_0^{I_B} \rho(I)\,dI} \tag{B.7}$$

we see that

$$k^{-1} = \int_0^{I_B} dI \frac{\exp\left[-\frac{1}{k_B T}(E(I)-E(0))\right]}{\gamma 2\pi k_B T} \int_I^{I_B} \frac{\omega(I')dI'}{I'} \exp\left[\frac{1}{k_B T}(E(I')-E(0))\right]. \tag{B.8}$$

Furthermore, we choose an energy gauge such that $E(0) = 0$, effectively defining the bottom of the metastable well as our zero-energy reference; B.8 then becomes equivalent to expression 4.48 from Hanggi *et al* [19]. We also recall that the integral $\int_{I_0}^{I_B} f(I)dI = \int_{E(I_0)}^{E(I_B)} f(E)\frac{dI}{dE}dE$ provided we can express f, E as functions of I. This allows us to express B.8 as:

$$k^{-1} = \int_0^{V_B} dE \frac{2\pi}{\omega(E)} \frac{\exp\left[-\frac{E}{k_B T}\right]}{\gamma k_B T} \int_E^{V_B} \frac{dE'}{I(E')} \exp\left[\frac{E}{k_B T}\right]. \tag{B.9}$$

Now if we make the assumption that $V_B \gg k_B T$ then it follows that $\exp\left[\frac{E}{k_B T}\right]$ varies much more rapidly than $I(E)$, and hence, the tail end of the above integrand (i.e. the E-values near V_B) will convey the lions share of the integral result. We then treat $I(E)$ in the second integrand as effectively constant at I_B. This yields:

$$k^{-1} = \int_0^{V_B} dE \frac{2\pi}{\omega(E)} \frac{\exp\left[-\frac{E}{k_B T}\right]}{\gamma k_B T} \frac{1}{I_B} \left[k_B T \left(\exp\left[\frac{E}{K_B T}\right]\right)\right]_{E=0}^{E=V_B}, \tag{B.10}$$

or equivalently

$$k^{-1} = \frac{2\pi}{\gamma I_B} \exp^{\left[\frac{V_B}{k_B T}\right]} \int_0^{V_B} \frac{dE \exp^{\left[-\frac{E}{k_B T}\right]}}{\omega(E)} \tag{B.11}$$

where we have assumed $\exp^{[\beta E_0]} = 1 \ll \exp^{[\beta V_B]}$ and can therefore be neglected.

By the same logic that allowed us to assume a constant $I(E) \to I_B$ in B.9 we can assume that the integral in B.10 will be dominated by E values near $E = 0$ (since the exponent is negative this time) and therefore assume a constant oscillatory frequency $\omega(E) \to \omega_0$, where ω_0 is the oscillation frequency at the bottom of the shallow well. Evaluating the integral in B.10 then results in

$$k^{-1} = \frac{2\pi k_B T}{\gamma I_B \omega_0} \exp^{\left[\frac{V_B}{k_B T}\right]} \left[- \exp^{\left[-\frac{V_B}{k_B T}\right]} - - \mathrm{e}^{[0]} \right], \tag{B.12}$$

Finally, taking the inverse gives us the rate of excitation over the potential barrier

$$k = \frac{\gamma I_B}{k_B T} \frac{\omega_0}{2\pi} \exp^{\left[-\frac{V_B}{k_B T}\right]} \tag{B.13}$$

Valid only when $V_B \gg k_B T$. This is the Kramer's escape rate cited in chapter 4

Appendix C

The escape rate using the IM-F method.

The following is derived mainly from the published work of Ingold [33, 34] with some additional details provided in areas of conceptual importance, and other details of arithmetic concern omitted; the purpose of this appendix is to establish the methodology in applying path integrals to deduce the partition function of an open quantum system.

We consider the influence functionals given in equation 5.42, and proceed by inserting the sum of actions given in equation 5.35 (from all of the bath modes) into the exponential of equation 5.18 and expressing it as a product (as in 5.42), we arrive at the *reduced* equilibrium density matrix

$$\langle q''|\rho_\beta|q'\rangle = \rho_\beta(q'',q') = \frac{1}{Z}\int_{q(0)=q'}^{q(\hbar\beta)=q''} Dq\mathrm{e}^{\left[-\mathrm{S^E[q]}/\hbar\right]}\mathrm{F[q]}. \tag{C.1}$$

Note that for our actual ensemble, the density matrix given in equation 5.18 would have dimensionality of $2+2N$ for all of the system and bath coordinates, and would take a form such as $W_\beta(q',q'',\vec{\mathbf{x}}',\vec{\mathbf{x}}'')$; equation C.1 amounts to taking a trace over the bath coordinates x' and x''.

To perform this trace, we follow the derivation of Ingold[33] and expand the position coordinates $x_i(\tau)$ in a Fourier series

$$x_i(\tau) = \sum_{n=-\infty}^{n=\infty} \xi_n \mathrm{e}^{[\mathrm{i}\nu_\mathrm{n}\tau]} \tag{C.2}$$

where ν_n are the Matsubara frequencies

$$\nu_n = n\frac{2\pi}{\hbar\beta}. \tag{C.3}$$

Note that each oscillator's classical trajectory must solve the classical equation of motion (since the oscillators assume a harmonic form, this is exact)

$$\ddot{x}_i^{cl}(\tau) - \omega_i^2 x_i^{cl}(\tau) = -\frac{c_i}{m_i} q, \tag{C.4}$$

an imaginary time analog to the classical equations of motion given in 5.26, however expression C.4 is obtained by variational calculus from seeking a stationary action. If we impose the boundary conditions $x_i^{cl}(0) = x_i^{cl}(\hbar\beta) = x_i$ we find a solution of the form

$$\begin{aligned} x_i^{cl}(\tau) &= \frac{\sinh(\omega_i \tau)}{\sinh(\hbar\beta\omega_i)} \left[x_i + \frac{c_i}{m_i\omega_i} \int_\tau^{\hbar\beta} d\sigma \sinh\left[\omega_i(\hbar\beta - \sigma) q(\sigma)\right] \right] \\ &+ \frac{\sinh\left[\omega_i(\hbar\beta - \tau)\right]}{\sinh(\hbar\beta\omega_i)} \left[x_i + \frac{c_i}{m_i\omega_i} \int_0^{\tau} d\sigma \sinh\left[\omega_i \sigma\right] \right]. \end{aligned} \tag{C.5}$$

Furthermore, if we seek to simplify the expression for the oscillator's classical action given in 5.39, we can perform partial integration on the product of $\int d\tau \dot{x}_i \dot{x}_i$ to obtain $x_i(\hbar\beta)\dot{x}_i(\hbar\beta) - x_i(0)\dot{x}_i(0) - \int d\tau x_i \ddot{x}_i$; we may then employ equation C.4 to cancel this latter expression against the potential terms of 5.39 leading us to rewrite equation 5.39 as:

$$S_i^{E,cl}[q, x_i] = \frac{m_i}{2}\left[x_i^{cl}(\hbar\beta)\dot{x}_i^{cl}(\hbar\beta) - x_i^{cl}(0)\dot{x}_i^{cl}(0)\right] + \int_0^{\hbar\beta} d\tau \frac{m_i}{2}\left[-\frac{c_i}{m_i} q x_i^{cl} + \frac{c_i^2}{m_i^2\omega_i^2} q^2\right] \tag{C.6}$$

If we insert the result of C.5 into C.6 (and then proceed through a certain amount of algebra which we omit here for brevity) we obtain an expression for the action of the oscillator

$$\begin{aligned} S_i^{E,cl}[q, x_i] &= m_i\omega_i \frac{\cosh(\hbar\beta\omega_i) - 1}{\sinh(\hbar\beta\omega_i)} (x_i - x^{(0)})^2 - \int_0^{\hbar\beta} d\tau \int_0^{\tau} d\sigma K_i(\tau - \sigma) q(\tau) q(\sigma) \\ &+ \frac{c_i^2}{2m_i\omega_i^2} \int_0^{\hbar\beta} d\tau q^2(\tau) \end{aligned} \tag{C.7}$$

where we have defined the integral kernel as

$$K_i(\tau) = \frac{c_i^2}{2m_i\omega_i}\frac{\cosh\left[\omega_i\left(\frac{\hbar\beta}{2}-\tau\right)\right]}{\sinh\left(\frac{\hbar\beta\omega_i}{2}\right)} = K_i(\hbar\beta-\tau). \tag{C.8}$$

In the above equation the following Fourier series expansion can be applied

$$\frac{\cosh\left[\omega_i\left(\frac{\hbar\beta}{2}-\tau\right)\right]}{\sinh\left(\frac{\hbar\beta\omega_i}{2}\right)} = \frac{2}{\hbar\beta}\sum_{l=-\infty}^{+\infty}\frac{\omega_i}{\omega_i^2+\nu_l^2}\mathrm{e}^{[\mathrm{i}\nu_l\tau]}, \tag{C.9}$$

hence:

$$\begin{aligned} K_i(\tau) &= \frac{c_i^2}{\hbar\beta m_i\omega_i}\sum_{l=-\infty}^{+\infty}\frac{\omega_i}{\omega_i^2+\nu_l^2}\mathrm{e}^{[\mathrm{i}\nu_l\tau]} \\ &= \frac{c_i^2}{\hbar\beta m_i\omega_i}\sum_{l=-\infty}^{+\infty}\mathrm{e}^{[\mathrm{i}\nu_l\tau]} - \frac{\mathrm{c_i^2}}{\hbar\beta\mathrm{m_i}\omega_\mathrm{i}}\sum_{\mathrm{l}=-\infty}^{+\infty}\frac{\nu_\mathrm{l}}{\omega_\mathrm{i}^2+\nu_\mathrm{l}^2}\mathrm{e}^{[\mathrm{i}\nu_l\tau]} \\ &= \frac{c_i^2}{m_i\omega_i}\sum_{j=-\infty}^{+\infty}\delta(\tau-j\hbar\beta) - k_i(\tau). \end{aligned} \tag{C.10}$$

We therefore define a new kernel as:

$$k_i(\tau) = \frac{c_i^2}{\hbar\beta m_i\omega_i^2}\sum_{l=-\infty}^{+\infty}\frac{\nu_l^2}{\nu_l^2+\omega_i^2}\mathrm{e}^{[\mathrm{i}\nu_l\tau]} \tag{C.11}$$

and exploit orthogonality and periodicity relations in $q(\tau)$ in conjunction with C.11, and C.10 to obtain:

$$\begin{aligned} S_i^{E,cl}[q,x_i] &= m_i\omega_i\frac{\cosh(\hbar\beta\omega_i)-1}{\sinh(\hbar\beta\omega_i)}\left(x_i-x^{(0)}\right)^2 - \int_0^{\hbar\beta}d\tau\int_0^{\tau}d\sigma k_i(\tau-\sigma)q(\tau)q(\sigma) \\ &- \frac{c_i^2}{2m_i\omega_i^2}\int_0^{\hbar\beta}d\tau\int_0^{\tau}d\sigma\delta(\tau-j\hbar\beta)q(\sigma)q(\tau) + \frac{c_i^2}{2m_i\omega_i^2}\int_0^{\hbar\beta}d\tau q^2(\tau) \\ &= m_i\omega_i\frac{\cosh(\hbar\beta\omega_i)-1}{\sinh(\hbar\beta\omega_i)}\left(x_i-x^{(0)}\right)^2 \\ &- \int_0^{\hbar\beta}d\tau\int_0^{\tau}d\sigma k_i(\tau-\sigma)\frac{-\left((q(\tau)-q(\sigma))^2-(q(\tau)^2+q(\sigma)^2)\right)}{2}. \end{aligned} \tag{C.12}$$

We further note that the quantum fluctuations of bath oscillator around the classical path yield a second order contribution to the action given by:

$$S_i^{E,(2)} = \int_0^{\hbar\beta} d\tau \frac{m_i}{2}(\dot{\xi}^2 + \omega_i^2 \xi_i^2) \tag{C.13}$$

and that this contribution is independent of x_i, thus yielding only a simple numerical factor. This factor can be captured (along with the first term of C.12) in the partition function of the single bath oscillator, by setting $c_i = 0 \forall i$. After some arithmetic work with the second term in expression C.12 we obtain the influence function of the bath oscillator:

$$F_i[q] = Z_i \mathrm{e}^{\left[-\frac{1}{2\hbar}\int_0^{\hbar\beta} \mathrm{d}\tau \int_0^{\hbar\beta} \mathrm{d}\sigma \mathrm{k_i}(\tau-\sigma)\mathrm{q}(\tau)\mathrm{q}(\sigma)\right]}. \tag{C.14}$$

Inspired by equation 5.42, we seek to express our sum of bath oscillator actions within the exponential argument above as a product, thereby redefining 5.42 more explicitly as

$$F[q] = \exp^{\left[-\frac{1}{2\hbar}\int_0^{\hbar\beta} d\tau \int_0^{\hbar\beta} d\sigma k(\tau-\sigma)q(\tau)q(\sigma)\right]}. \tag{C.15}$$

To determine $k(\tau)$ we observe that our single oscillator kernel just so happens to look very much like a Laplace transform $\hat{\gamma}(z)$ of the original damping kernel $\gamma(t)$, as defined in 5.32.

$$\begin{aligned} \hat{\gamma}(z) &= \int_0^{\infty} dt \mathrm{e}^{[-\mathrm{tz}]}\gamma(\mathrm{t}) = \int_0^{\infty} \mathrm{dt}\mathrm{e}^{[-\mathrm{tz}]}\frac{2}{\mathrm{M}}\int_0^{\infty}\frac{\mathrm{d}\omega}{\pi}\frac{\mathrm{J}(\omega)}{\omega}\cos(\omega\mathrm{t}) \\ &= \frac{2}{M}\int_0^{\infty}\frac{d\omega}{\pi}\frac{J(\omega)}{\omega}\frac{z}{z^2+\omega^2} \end{aligned} \tag{C.16}$$

and hence, $k(\tau) = \sum_{i=1}^{N} k_i(\tau)$ can be expressed more succinctly as

$$k(\tau) = \frac{M}{\hbar\beta}\sum_{n=-\infty}^{\infty} |\nu_n|\hat{\gamma}(|\nu_n|)\mathrm{e}^{[\mathrm{i}\nu_\mathrm{n}\tau]}. \tag{C.17}$$

Thus we fully determine the net effect of the dissipative path on the system. Considering the entirety of the above discussion, the effective Euclidean action to be minimized in equations 5.18 and 5.19 is

$$S_{eff}^{(E)}[q] = \int_0^{\hbar\beta} d\tau \left(\frac{1}{2}m\dot{q}(\tau) + V(q(\tau))\right) + \frac{1}{2}\int_0^{\hbar\beta} d\tau \int_0^{\tau} d\tau' k(\tau-\tau')(q(\tau)-q(\tau'))^2. \tag{C.18}$$

We now make the substitution

$$q(\tau) = q_{cl}(\tau) + \xi(\tau) \tag{C.19}$$

Where $\xi(\tau)$, the quantum fluctuation about the classical path, can be expanded in a Fourier series

$$\xi(\tau) = \sum_{n=-\infty}^{+\infty} \xi_n \mathrm{e}^{[\mathrm{i}\nu_n\tau]} \tag{C.20}$$

which is assured to sum to zero at both endpoints $\tau = 0$, and $\tau = \hbar\beta$ as required. If we substitute C.19 into C.18 we obtain:

$$\begin{aligned} S_{eff}^{(E)}[q] = &\int_0^{\hbar\beta} d\tau \left[\frac{M}{2}\dot{q_{cl}}^2(\tau) + V(q_{cl}(\tau)) + \frac{1}{2}\int_0^{\tau} d\tau' k(\tau-\tau')(q_{cl}(\tau)-q_{cl}(\tau'))\right] \\ &+ \int_0^{\hbar\beta} d\tau \left[\frac{M}{2}\dot{\xi}^2(\tau) + V(q_{cl}(\tau))\xi^2 + \frac{1}{2}\int_0^{\tau} d\tau' k(\tau-\tau')(\xi(\tau)-\xi(\tau'))^2\right]. \end{aligned} \tag{C.21}$$

According to 5.19, we require periodic paths to contribute to the partition function. We note the periodic paths for this action in the inverted potential: (1) resting precariously at the top of the left extrema ($q = 0$), (2) resting at the minimum (q_B) indefinitely, and (3) beginning at the top of the left maxima, proceeding right until stopping at the same height on the slope, and returning, adiabatically to the left maxima. The latter path is referred to as the 'bounce', or 'instanton' action, and contributes only below the crossover temperature, a region we will not concern ourselves with, since the thermally averaged tunnelling rate accounts for this region.

If we substitute the first scenario (i.e. $q = 0 \ \forall \ t$) into C.21 we obtain

$$S_1^E = \frac{M\hbar\beta}{2} \sum_{n=-\infty}^{\infty} \left(\nu_n^2 + |\nu_n|\hat{\gamma}(|\nu_n|) + \omega_0^2\right)|\xi_n^2| \tag{C.22}$$

whereas if we substitute the second scenario (i.e. $q = q_B \ \forall \ t$) into C.21 we obtain:

$$S_2^E = \hbar\beta V_b + \frac{M\hbar\beta}{2} \sum_{n=-\infty}^{\infty} \left(\nu_n^2 + |\nu_n|\hat{\gamma}(|\nu_n|) - \omega_b^2\right) |\xi_n^2|, \tag{C.23}$$

an expression which can be further simplified by constraining ξ_n to ensure real paths; hence we set $\xi_n = a_n + \mathrm{ib_n}$ with $a_n = a_{-n}$, and $b_{-n} = -b_n$. Thus

$$S_1^E = \frac{M\hbar\beta}{2} \left(\nu_0^2 + |\nu_0|\hat{\gamma}(|\nu_0|) + \omega_0^2\right) |\xi_0|^2 + \frac{M\hbar\beta}{2} \sum_{n\neq 0}^{\infty} \left(\nu_n^2 + |\nu_n|\hat{\gamma}(|\nu_n|) + \omega_0^2\right) |\xi_n|^2. \tag{C.24}$$

Similarly, equation C.23 becomes

$$S_2^E = \hbar\beta V_b + \frac{M\hbar\beta}{2} \left(\nu_0^2 + |\nu_0|\hat{\gamma}(|\nu_0|) - \omega_b^2\right) |\xi_0|^2 + \frac{M\hbar\beta}{2} \sum_{n\neq 0}^{\infty} \left(\nu_n^2 + |\nu_n|\hat{\gamma}(|\nu_n|) - \omega_b^2\right) |\xi_n|^2. \tag{C.25}$$

Note that we have separated the $n = 0$ terms from the summation in the above relations since from C.3 we see that $\nu_0 = 0$; this will be useful shortly. At this point we are reminded that the path integrals indicated in equation 5.19 take place over *all* positions q during the process. and hence, in Fourier representation, we have still to integrate over the possible values of each ξ_n in equation C.23. Recall that a Gaussian integral is calculated in general using:

$$I(a) = \int_{-\infty}^{\infty} \mathrm{dx e^{-ax^2}} = \sqrt{\frac{\pi}{\mathrm{a}}} \tag{C.26}$$

Our final partition function is then:

$$
\begin{aligned}
Z &= \oint Dq\mathrm{e}^{\left[-\mathrm{S^E[q]}/\hbar\right]}. = \oint\limits_{\mathrm{q=0}} \mathrm{Dqe}^{\left[-\mathrm{S^E[q]}/\hbar\right]} + \oint\limits_{\mathrm{q=q_b}} \mathrm{Dqe}^{\left[-\mathrm{S^E[q]}/\hbar\right]} \\
&\approx \int \mathrm{d}\xi_\mathrm{o}\mathrm{d}\xi_1\mathrm{d}\xi_2\ldots\mathrm{e}^{\left[\frac{\mathrm{M}\beta}{2}\omega_0^2|\xi_0|^2+\mathrm{M}\beta\sum_{\mathrm{n=1}}^{\infty}\left(\nu_\mathrm{n}^2+|\nu_\mathrm{n}|\hat{\gamma}(|\nu_\mathrm{n}|)+\omega_0^2\right)|\xi_\mathrm{n}|^2\right]} \\
&+ \int \mathrm{d}\xi_\mathrm{o}\mathrm{d}\xi_1\mathrm{d}\xi_2\ldots\mathrm{e}^{\left[\frac{\mathrm{M}\beta}{2}(-\omega_\mathrm{b}^2)|\xi_0|^2+\mathrm{M}\beta\sum_{\mathrm{n=1}}^{\infty}\left(\nu_\mathrm{n}^2+|\nu_\mathrm{n}|\hat{\gamma}(|\nu_\mathrm{n}|)+\omega_0^2\right)|\xi_\mathrm{n}|^2\right]} \\
&= \sqrt{\frac{\pi}{\frac{M\beta\omega_0^2}{2}}}\prod_{n\neq 0}\sqrt{\frac{\pi}{\frac{M\beta}{2}\left(\nu_n^2+|\nu_n|\hat{\gamma}(|\nu_n|)+\omega_0^2\right)}} \\
&+ e^{-\beta V_b}\sqrt{\frac{\pi}{\frac{M\beta(-2\omega_b^2)}{2}}}\prod_{n\neq 0}\sqrt{\frac{\pi}{\frac{M\beta}{2}\left(\nu_n^2+|\nu_n|\hat{\gamma}(|\nu_n|)-\omega_b^2\right)}} \\
&= \frac{1}{\omega_0}\sqrt{\frac{2\pi}{M\beta}}\prod_{n=1}\frac{\pi}{\frac{M\beta}{2}\left(\nu_n^2+|\nu_n|\hat{\gamma}(|\nu_n|)+\omega_0^2\right)} \\
&- \frac{\mathrm{i}}{2\omega_b}e^{-\beta V_b}\sqrt{\frac{2\pi}{M\beta}}\prod_{n=1}\frac{\pi}{\frac{M\beta}{2}\left(\nu_n^2+|\nu_n|\hat{\gamma}(|\nu_n|)-\omega_b^2\right)}. \qquad \text{(C.27)}
\end{aligned}
$$

As shown in equation 5.44 (Note, we have actually *cheated* somewhat in this derivation, since Gaussian integrals of the form given in equation C.26 cannot be performed for $a < 0$ as in the case of the third line of 5.44 where a takes the value $-\omega_b^2$. This problem is rectified by taking an analytic continuation of the integral along the 'direction of steepest descent' that is to say, along the imaginary axis. The result is essentially the same with an additional factor of $\frac{1}{2}$.)

Appendix D

Computational challenges.

The bulk of time and effort that this project required was spent scanning through the parameter space of the variables available to the system. A single detection simulation for a given frequency, barrier height, pulse width, and quality factor could take a single processor as long as 1 day, if the Q-value of that iteration was particularly large (since the decay process takes place at a rate proportional to $\frac{1}{Q}$, this made thorough scans of the high Q and high σ region of parameter space difficult.) Initial coarse scans involved sampling 20 values of σ, and 5 values of Q over 40 different potentials, each with their own characteristic V_B

After scanning out the three dimensional Q-σ-V_B space roughly, a region of local maximum fidelity began to emerge, which seemed to rely on a combination of excitation and tunnelling through a low-Q, short σ process. It remains entirely possible that other regions of parameter space relying more heavily on excitation and decay could evince a seperate local maximum of improved detection fidelity, most likely at a longer pulse width.

To give an idea of the computational demands of this project, figure D.1 shows a plot of the average use of computer resources on SHARCNET. This was only one of two SHARCNET accounts being used for this project, as well as the SGI computers at the physics department at Dalhousie University. There were, at times, over 3024 CPU-hours being devoted to this project per day.

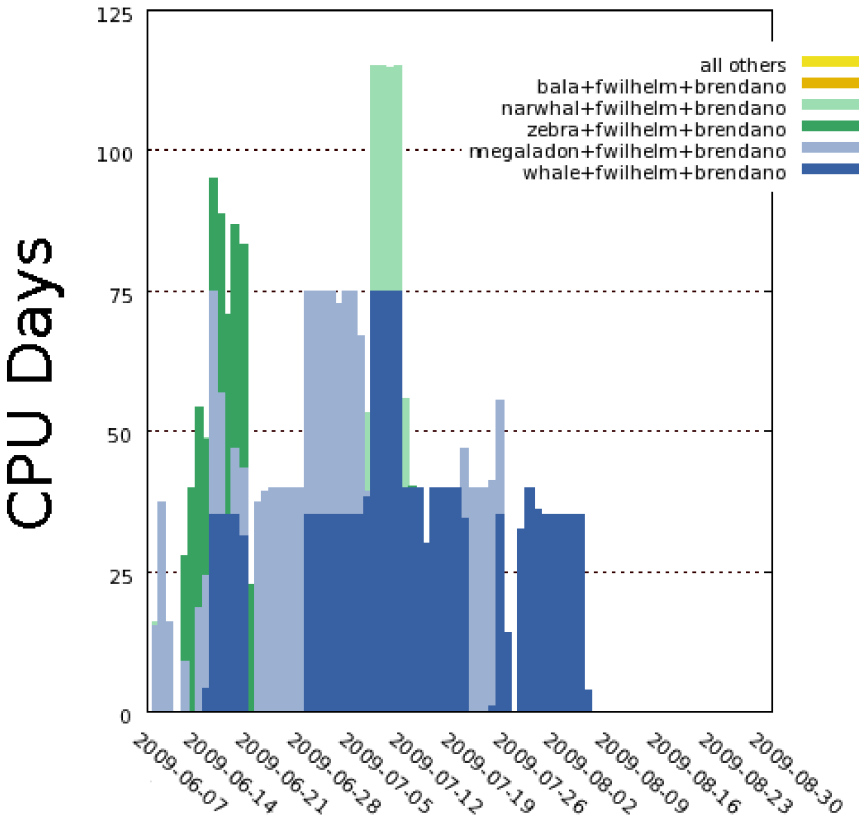

Figure D.1: CPU-hours consumed per day, on one account devoted to scanning out parameter space for this project for the period from May through July 2009.

References

[1] M.H. Devoret, J. M. Martinis, and J. Clarke. Measurements of macroscopic quantum tunneling out of the zero-voltage state of a current-biased josephson junction. *Physical Review Letters*, 55:1908–1911, 1985. 1

[2] John M. Martinis and Michel H. Devoretand John Clarke. Energy-level quantization in the zero-voltage state of a current-biased josesphson junction. *Physical Review Letters*, 55(15):1543–1546, 1985. 1

[3] J. Clarke, A. Cleland, M. Devoret, D. Esteve, and J. Martinis. Quantum mechanics of a macroscopic variable: The phase difference of a josephson junction. *Science*, 239:992–997, 1988. 1

[4] R. J. Schoelkopf and S. M. Girvin. Wiring up quantum systems. *Nature*, 451:664–669, 2008. 1

[5] F. K. Wilhelm and E. Solano. Photon lab in a circuit. *Nature*, 445:500, 2007. 1

[6] M.H. Devoret and J. M. Martinis. Implementing qubits with superconducting integrated circuits. *Quantum Information Processing*, 3:163–203, 2004. 1, 16

[7] A. A. Houck, D. I. Schuster, J. M. Gambetta, J. A. Schreier, B. R. Johnson, J. M. Chow, J. Majer, L. Frunzio, M. H. Devoret, S. M. Girvin, and R. J. Schoelkopf. Generating single microwave photons in a circuit. *Nature*, 449:328–331, 2007. 1, 66

[8] Y. Makhlin, G. Schon, and A. Shnirman. Quantum-state engineering with josephson-junction devices. *Reviews of Modern Physics.*, 73:357–400, 2001. 1

[9] I Chiorescu, P. Bertet, K. Semba, Y. Nakamura, C.J.P.M. Harmans, and J.E. Mooij. Coherent dynamics of a flux qubit coupled to a harmonic oscillator. *Letters to Nature*, 431:159–162, 2004. 1

[10] J. Gambetta, A. Blais, M. Boissonneault, A. A. Houck, D. I. Schuster, and S. M. Girvin1. Quantum trajectory approach to circuit qed: Quantum jumps and the zeno effect. *Phys. Rev. A, 012112 (2008) [18 pages]*, 77:1–18, 2008. 1, 16

[11] A. Wallraff, D. I. Schuster, A. Blais, L. Frunzio, R.-S. Huang, J. Majer, S. Kumar, S. M. Girvin, and R. J. Schoelkopf. Strong coupling of a single photon to a superconducting qubit using circuit quantum electrodynamics. *Nature*, 431:162–167, 2004. 1

[12] Alexandre Blais, Ren-Shou Huang, Andreas Wallraff, S. M. Girvin, and R. J. Schoelkopf. Cavity quantum electrodynamics for superconducting electrical circuits: An architecture for quantum computation. *Physical Review A*, 69, 2004. 1

[13] Michael Mück, J. B. Kycia, and John Clarke. Superconducting quantum interference device as a near-quantum-limited amplifier at 0.5 ghz. *Applied Physics Letters*, 78(7), 2001. 1

[14] M. A. Castellanos-Beltran and K. W. Lehnert. Widely tunable parametric amplifier based on a superconducting quantum interference device array resonator. *Applied Physics Letters*, 91:083509, 2007. 1

[15] G. Romero, J. J. Garcia-Ripoll, and E. Solano. Microwave photon detector in circuit qed. *Physical Review Letters*, 102:173602, 2009. 1, 2, 54

[16] Claude Cohen-Tannoudji. *Atom Photon Interactions: Basic Processes and Applications.* John Wiley & Sons., New York, N.Y., U.S.A., 1992. 2, 3, 4, 66

[17] D.T. Colbert and W. H. Miller. A novel discrete variable representation for quantum mechanical reactive scattering via the s-matrix kohn method. *Journal of Chemical Physics*, 96:1982–1991, 1992. 2, 20, 21, 66

[18] L. D. Landau, E. M. Lifshitz, J.B. translated by Sykes, and J.S. Bell. *Mechanics -Third edition.*, chapter 1 of Course of Theoretical Physics. Butterworth-Heinemann., Oxford, reprinted 1991. 2, 25, 27

[19] P. Hänggi, P. Talkner, and Borkovec M. Reaction-rate theory: fifty years after kramers. *Reviews of Modern Physics*, 62-2:251–342, 1990. 2, 25, 32, 33, 35, 73

[20] H.A. Kramers. Brownian motion in a field of force and the diffusion model of chemical reactions. *Physica (Utrecht)*, 62-2:284–304, 1940. 2, 25, 35

[21] H. Risken. *The Fokker-Planck Equation; Methods of Solution and Applications. Second Edition.* Springer-Verlag, Berlin, 1996. 3

[22] S. Haroche and J.M. Raimond. *Exploring the Quantum; Atoms, Cavities, and Photons.* Oxford University Press, Oxford, U.K., 2006. 6, 16

[23] J. M. Galassi, J. Davies, B. Theiler, G. Gough, P. Jungman, M. Booth Alken, and F. Rossi. *GNU Scientific Library Reference Manual (3rd Ed.).* Network Theory Limited, 2009. 8

[24] M. Devoret. *Quantum Fluctuations in Electrical Circuits.*, chapter 10 of Les Houched, Session LXIII. Elsevier-Science., Gif-sur-Yvette, France, 1995. 14

[25] A.I. Larkin and Yu. N. Ovchinnikov. Effect of level quantization on the lifetime of metastable states. *Soviet journal of physics -JETP*, 64:185–189, 1986. 16, 54

[26] M. Mariantoni, M.J. Storcz, F.K. Wilhelm, W.D. Oliver, A. Emmert, A. Marx, R. Gross, H. Christ, and E. Solano. On-chip microwave fock states and quantum homodyne measurements. *arxiv*, 2006. 16

[27] M. Neeley, M. Ansmann, R. C. Bialczak, M. Hofheinz, N. Katz, E. Lucero, A. Oconnell, H. Wang, A. N. Cleland, and J. M. Martinis. Process tomography of quantum memory in a josephson-phase qubit coupled to a two-level state. *Nature Physics*, 4:523–526, 2008. 16, 39

[28] Matthias Steffen, M. Ansmann, R. McDermott, N. Katz, Radoslaw C. Bialczak, Erik Lucero, Matthew Neeley, E. M. Weig, A. N. Cleland, and John M. Martinis. State tomography of capacitively shunted phase qubits with high fidelity. *Physical Review Letters*, 97:050502, 2006. 16, 39

[29] Devendra K Misra. *Radio-Frequency and Microwave Communication Circuits Analysis and Design.* John Wiley & sons, Inc., Toronto, Ontario, 2001. 16, 56

[30] Diego Dominici. Asymptotic analysis of the hermite polynomials from their differential-difference equation. *arXiv:math/0601078v1 [math.CA]*, 1:500, 2006. 19

[31] C. W. Gardiner. *Handbook of Stochastic Methods.* Springer-Verlag, Berlin, 2004. 25

[32] I.S. Gradshteyn and I.M. Ryzhik. *Table of Integrals, Series, and Products.* 5^{th} edition Academic Press, San-Diego, California, 2007. 37

[33] Gert-Ludwig Ingold. *Dissipative Quantum Systems.*, chapter 4 of Quantum transport and dissipation . Vch Publishers, Oxford, 1998. 43, 75

[34] Gert-Ludwig Ingold. *Path Integrals and Their Applications to Dissipative Quantum Systems.* Springer Berlin / Heidelberg, 2008. 43, 75

[35] Ulrich Weiss. *Quantum Dissipative Systems, 2nd edition.* World Scientific publishing., Hackensack, NJ, 1999. 47

[36] K.S. Chow, D. A. Browne, and V. Ambegaokar. Quantum kinetics of a superconducting tunnel junction: Theory and comparison with experiment. *Physical Review B*, 17-4:1624–1646, 1988. 54, 55

[37] K.S. Chow and V. Ambegaokar. Transition from quantum to classical dissipation in the problem of escape from a metastable well: Application to josephson junctions. *Physical Review B*, 38-16:11168–11176, 1988. 54, 55

[38] David M. Pozar. *Microwave Engineering -2nd edition.* John Wiley & sons, Inc., Toronto, Ontario, 1994.

[39] Alexandre Blais, Ren-Shou Huang, Andreas Wallraff, S. M. Girvin, and R. J. Schoelkopf. Cavity quantum electrodynamics for superconducting electrical circuits: An architecture for quantum computation. *Physica Review A*, 69:062320, 2004.

[40] Claude Cohen-Tannoudji. *Quantum Mechanics.* John Wiley & Sons., Toronto, Ontario, Canada, 2004.